

Nutrients and plankton spatial distributions induced by a coastal eddy in the Gulf of Lion. Insights from a numerical model.

Rose Campbell^{a,b}, Frédéric Diaz^{a,c}, ZiYuan Hu^a, Andrea Doglioli^a, Anne Petrenko^a, Ivan Dekeyser^a

^a*Aix-Marseille Université, Université du Sud Toulon-Var, CNRS/INSU, IRD, MIO UM 110, 13288, Marseille, Cedex 09, France*

^b*ACRI-ST, 260 Route du Pin Montard, BP 234 06904 Sophia Antipolis, France*

^c*Tel: +33(0)491829337*

Fax: +33(0)491829540

frederic.diaz@univ-amu.fr

Abstract

A plankton functional types model forced by a hydrodynamic model is used in the present work to study the impacts of a coastal eddy on the distribution of nutrients and plankton in the western part of Gulf of Lion (NW Mediterranean Sea). This study, based on a realistic simulation of the year 2001, focuses on a long-life anticyclonic eddy detected during summer. The studied anticyclonic eddy has some biogeochemical characteristics of those observed in the open ocean as for example the low productivity at their core and rising-up of nutricline on their edges. However the functioning and consequences of such coastal eddy on nutrients and plankton distributions are complicated by potential interactions with topography, wind-induced upwelling along the Languedoc Coast and nearby Northern Current (NC). Especially the proximity of the southern edge of the eddy with the NC makes possible the exchanges of organic matter (*e.g.* plankton) at times during the eddy's life. The coastal eddy thus transports organic matter from the coastal zone to the offshore domain. The coupled model also suggests the importance of

offshore-to-coastal transport by NC through a seeding process of the eddy in plankton at the beginning of its life.

A detailed biogeochemical functioning of the studied eddy all along its lifetime is proposed from the model results. At the beginning the eddy mainly acts as a transporter of the plankton wind-induced bloom occurring along the Languedoc Coast several days before the eddy set up. At the same time the eddy shows upwards vertical velocities on its edges creating upwelling of nutrient-enriched waters. The process of eddy-induced upwelling is notably enhanced on the eddy western side along the Roussillon Coast due to the shelf topography. The around-eddy advection and relative lower temperatures prevent the large development of phytoplankton along the Roussillon Coast and the eddy-induced bloom is predicted to occur near the north-western side of the eddy. The eddy-induced and wind-induced blooms of phytoplankton then merge on the eastern side by advection and this process of aggregation may explain the persistent occurrence of a filament of high chlorophyll observed on the offshore edge of the eddy throughout the study period. The changes in plankton composition due to a combination of top-down and bottom-up processes during the coast-to-offshore transport may explain the disappearance of the filament south of 43°N at the surface.

Keywords:

Nutrients and plankton distributions, coastal eddy, upwelling, Gulf of Lion, Mediterranean Sea

1. Introduction

Eddies and the physical-biogeochemical processes linked to these structures have been intensively studied in the open ocean for the past decade. Their functioning and impacts on the regional and global biogeochemical cycles (Siegel et al., 1999; Oschlies, 2002; Sweeney et al., 2003) are starting to be well understood (see also the E-FLUX and EDDIES programmes,

special volume Deep-Sea Research II, 55, 2008). Eddies play a key role in ocean dynamics, heat transport and biogeochemical budgets through intense upwelling of nutrients, subduction of plankton and horizontal stirring (see review of Lévy, 2008). With appropriate spatial resolution, numerical studies also show the importance of these processes, particularly when coupled to biogeochemical models, at the scales of ocean basins (Oschlies and Garçon, 1998; McGillicuddy et al., 1998; Eden and Dietze, 2009) or fronts (Franks and Walstad, 1997; Lévy, 2003). Crucial questions as for example the influence of eddies on the soft-tissue carbon pump (Omta et al., 2007) or on the long-term evolution of marine ecosystems (Sasai et al., 2010) have been recently addressed using coupled modelling.

While numerous in the open ocean (McGillicuddy et al., 1998, and references therein; Martin and Richards, 2001; Martin and Pondaven, 2003), studies of eddy dynamics and their biogeochemical impacts in the coastal domain are globally much more scarce. However the number of coastal-eddy studies has been increasing for several years. In the region of western Australia, Moore II et al. (2007) and Dietze et al. (2009) have shown the crucial role of eddies generated from coastal jet in the cross-shelf exchanges of phytoplankton by experimental and numerical studies, respectively. Recently, an integrated study of the eddies associated to the East Australian Current (*e.g.* Suthers et al., 2011) has shown consequences of generation and evolution of coastal eddies on the end-to-end ecosystem of the New South Wales Coast. Other studies such as that of Calado et al. (2010) highlight the ability of a coastal eddy to induce strong upwelling involving potential increase of biological productivity on the Southeast Brazil continental margin.

To our knowledge, in the literature, no similar studies have been done in the Northwestern Mediterranean Sea (NWMS). Millot (1979, 1982) however inferred the presence of coastal recirculation in the western part of Gulf of Lion from current measurements and satellite images. More recently (Hu

et al., 2009, 2011a; Kersalé et al., submitted) confirmed the Millot's observations with new *in situ* measurements and numerical modelling. Observations of coastal eddies have also been made in the eastern part of the gulf of Lion (Allou et al., 2010) and in the Catalan Sea (Tintoré et al., 1990; Rubio et al., 2009; Garreau et al., 2011). In the Gulf of Lion particularly, ocean colour studies using remote sensors, from CZCS to the most recent MERIS, have synoptically revealed strong spatial variations of chlorophyll (Demarcq and Wald, 1984; Bosc et al., 2004; Forget and André, 2007) and suspended matter (Forget and Ouillon, 1998; Forget et al., 2001; Reffray et al., 2004) concentrations down to the submesocale (2-20 km, *sensu* Lévy, 2008). The spatial variability of biogeochemical properties mainly appears in the form of filaments, fronts, meanders and eddies (Bosc et al., 2004; Forget and André, 2007; Hu et al., 2009). The Gulf of Lion is characterized by its strong northerly and northwesterly winds, known locally as the Mistral and Tramontane, that frequently generate upwellings and downwellings along the coast (Millot, 1990) as well as transient processes such as currents, eddies and dense water formation on the Gulf of Lion shelf (Petrenko, 2003; Dufau-Julliand et al., 2004; Ulses et al., 2008; Hu et al., 2009). Several rivers including the most important one, the Rhône, provide the Gulf of Lion with fresh water and a year-round supply of important quantities of nutrients and organic matter (Ludwig et al., 2009). These river runoffs influence the pelagic ecosystem of the Gulf of Lion and also the biogeochemistry of the NW Mediterranean basin (Minas and Minas, 1989; Moutin et al., 1998; Auger et al., 2011). Depending on their spatial extent and shape the freshwater plumes can thus interact with another important hydrodynamic feature of the area, the Northern Current (NC) (Millot, 1990). This current is associated with strong mesoscale instabilities in the form of meanders, eddies and filaments (Sammari et al., 1995; Durrieu de Madron et al., 1999; Flexas et al., 2002) and usually flows along the shelf break of the Gulf of

Lion from the Ligurian Sea to the Catalan Sea but can occasionally partially penetrate the continental shelf (Petrenko, 2003; Petrenko et al., 2005). The NC is generally characterized by low nutrient contents, a deep nutricline and low year-round biological activity (Lefèvre et al., 1997). These biogeochemical features are in contrast to continental-origin water masses. When the NC water masses interact with those of the shelf during episodes of intrusions (Petrenko et al., 2005) or when eddies are generated from the NC meanders (Diaz et al., 2000) the spatial variability of biogeochemical properties and processes is notable.

The present work lies in the framework of the LAgrangian Transport EXperiment (LATEX) project (2008-2011) launched to study the role of mesoscale eddies on the shelf-offshore exchanges in the Gulf of Lion. A set of recent works by Hu et al. (2009, 2011a,b) has increased our knowledge on the physical dynamics of the coastal eddies occurring in the western part of the Gulf of Lion (Fig. 1). The objective of the present work is to characterize the biogeochemical functioning of such eddies, and, especially, to highlight the induced nutrient and plankton spatial distributions in the western Gulf of Lion. To fulfill this objective the main tool used here is a physical-biogeochemical numerical model that enables a combined analysis of interactions between the various hydrodynamic and biogeochemical processes occurring in the eddy. The study especially focuses on a coastal anticyclonic eddy which was detected using realistic numerical modelling during the summer of 2001 (Hu et al., 2009).

2. Method

2.1. Model Description

The physical model used in this study is Symphonie (Estournel et al., 2003; Marsaleix et al., 2008), a 3-D primitive equation, free surface model, based on hydrostatic and Boussinesq approximations. This model has already

been used to simulate the wind-induced circulation, episodes of dense water formation and intrusion of the NC onto the continental shelf (Dufau-Julliand et al., 2004; Petrenko et al., 2005; Ulses et al., 2008). The Symphonie version used in this study was developed by Hu et al. (2009) which improved the advection-dispersion algorithm for a better representation of submesoscale in the Gulf of Lion.

The biogeochemical model was constructed using the Eco3M modeling platform (Baklouti et al., 2006a,b). This modular and mechanistic platform for biogeochemical modelling was recently used to represent a stage structured population model of the copepod *Centropages typicus* applied to the northwestern Mediterranean (Eisenhauer et al., 2009) and also to explain some specificities of biogenic elements stoichiometry in the Mediterranean Sea (Mauriac et al., 2011).

The biogeochemical model is a multi-nutrient and multi-plankton functional types model that simulates the dynamics of several biogeochemical decoupled cycles of biogenic elements (carbon, nitrogen, phosphorus and silica) and non-redfieldian plankton groups. The model structure used in this study is mostly based on the pelagic plankton ecosystem model recently developed for the Northwestern Mediterranean basin by Auger et al. (2011).

Some changes have however been made to Auger et al. (2011)'s version. These modifications deal with the protist grazers (nano- and microzooplankton) and heterotrophic bacteria compartments. In Auger et al. (2011)'s version the heterotrophs (from bacteria to mesozooplankton) were represented by the Anderson and Pondaven (2003) model with the main characteristic of homeostatic regulation of elemental composition. While this assumption can be acceptable for mesozooplankton such as copepods (Urabe and Watanabe, 1992; Sterner and Robinson, 1994), laboratory and field experiments (Putt and Stoecker, 1989; Eccleston-Parry and Leadbeater, 1995; Vrede et al., 2002; Makino et al., 2003) do not clearly show this physiological balance for unicel-

lular heterotrophs. On the whole, field studies suggest that the physioecology (growth rate) of proto-zooplankton are closer to that of phytoplankton than that of mesozooplankton (Hirst and Bunker, 2003; Le Quéré et al., 2005). Therefore we have chosen to represent the protist grazers and heterotrophic bacteria processes, especially the terms of exudation, uptake/excretion of dissolved organic/inorganic matter, similarly to that of phytoplankton as recently proposed by Baklouti et al. (2011). Other changes deal with the reduction of the particulate organic matter to one compartment both for the sake of simplicity and because the modelled pattern of size classes of particles are often difficult to validate due to a lack of corresponding *in situ* data sets. The last modification concerns the use of a more realistic temperature function for phytoplankton functional types which is the thermo-inhibition curve of Eppley (1972). All the equations and processes modified with regards to the Auger et al. (2011)'s version as well as parameter values are presented in Appendix A. A schematic diagram is shown in the Figure 2.

2.2. Model Implementation

2.2.1. Coupling Technique

The Hu et al. (2009)'s version of Symphonie calculates the advection and diffusion of the biogeochemical tracers, while the biogeochemical model computes the temporal variations of these quantities due to biological processes. The spatial and temporal variations of the biogeochemical tracers (C) are governed by the conservation equation for which the horizontal diffusion of tracer is neglected :

$$\frac{\partial C}{\partial t} + \frac{\partial uC}{\partial x} + \frac{\partial vC}{\partial y} + \frac{\partial(w - w_s)C}{\partial z} = \frac{\partial}{\partial z} \left(K_v \frac{\partial C}{\partial z} \right) + \xi_{bio} \quad (1)$$

Where (u , v , w) are the mean current velocity components, w_s is the sinking velocity of particulate organic matter and microphytoplankton, K_v

is the vertical turbulent diffusion coefficient obtained with the parameterization of Gaspar and Lefevre (1990), and ξ_{bio} is the source/sink term for the biogeochemical variables. To limit computation time, the hydrodynamic model is run independently, with a barotropic time step of 6 seconds. The outputs (temperature, velocity, surface elevation, and vertical diffusion) are averaged over periods of 17 hours (local inertial period) and saved. These results are subsequently read by the biogeochemical model, which has a time step of 1 hour.

2.2.2. Grid, Initial and Boundary Conditions

The modelled zone extends over the Gulf of Lion and part of the Ligurian and Catalan Seas, measuring 711 by 303 km. The study zone is centred on the western part of the Gulf of Lion as indicated in Figure 1. The grid is rotated 31° counter-clockwise from true north, and uses a square horizontal mesh with a resolution of 3 km. Sigma coordinates were used on the vertical with a maximum of 40 vertical levels. The model was run for the year 2001. The initial conditions for the variables of the biogeochemical model are provided by numerical fields of a larger-scale physical-biogeochemical model, OPATM-BFM (Lazzari et al., 2011), interpolated for all biogeochemical variables on the Symphonie model grid. Tests were conducted by integrating the total quantity of carbon, nitrogen and phosphorus in the domain volume in order to determine the spin-up period of the model. Due to the open boundary conditions, none of the total quantities are strictly conservative, but we consider the spin-up period to be over when the total carbon in the model reaches a maximum and begins to stabilize. The period lasts around 100 days, therefore model results can be studied from April 15th, 2001 onwards. Six rivers are taken into account by the model (Fig. 1): the petit Rhône, the grand Rhône, the Hérault, the Orb, the Aude and the Ebro, which is outside the Gulf of Lion. Daily measurements of river discharge rates provided

by the Banque Hydrologique de France (2010) are interpolated to each time step of the model. River temperature is prescribed by a sinusoidal function based on a 20-years climatology of river temperature from the Rhône (Banque Hydrologique de France, 2010). Monthly measured concentrations of biogeochemical model variables as ammonium (NH_4), nitrate (NO_3), phosphate (PO_4) and dissolved organic carbon (DOC) are daily interpolated from Ludwig et al. (2009). The other variables are not available from *in situ* data and hence have been derived from empirical relationships. Silicate concentrations (H_3SiO_4) are derived from the measured nitrate concentrations using the ratio 1:1.4 reported by Moutin et al. (1998). Dissolved organic nitrogen (DON) and phosphorus (DOP) river concentrations are respectively calculated from total nitrate (NO_3) and phosphate (PO_4) concentrations using robust empirical $NO_3:TN$ and $PO_4:TP$ ratios established for the Rhône (Ludwig et al., 2009). Particulate organic carbon (POC) contents are calculated from an empirical linear relationships between organic suspended matter and Rhône runoffs (Sempéré et al., 2000). Particulate organic nitrogen (PON) and phosphorus (POP) contents are derived from POC data using the constant ratios of $POC:PON=11.3$ and $POC:POP=106.9$ measured in the Rhône River for the 2007-2008 period (Raimbault, unpubl. data). The study of Moutin et al. (1998) also provides an estimate of particulate chlorophyll detritus ($POChl$) inputs (~ 3.7 mg Chl m^{-3}) to the open sea resulting from the osmotic lysis of freshwater phytoplankton species at the river mouth. Marine zooplankton, phytoplankton and bacteria are considered to be absent from the river inputs. Riverine zooplankton, phytoplankton and bacteria biomasses are included in the particulate organic pool described above. Due to the absence of data concerning riverine biogenic silica ($POSi$) inputs to the Gulf of Lion, $POSi$ is fixed at a constant value of 28 $mmol\ m^{-3}$ averaged from concentrations measured in the world's largest rivers (Conley, 1997). This data set is linearly interpolated to each modelled day.

The open boundaries conditions, to the west and south of the model domain, are derived from the 10-day averaged numerical fields of the OPATM-BFM (Lazzari et al., 2011) model and used to assign values to the biogeochemical tracers in case of advection into the modelled domain.

2.3. Satellite data

2.3.1. Ocean color data

Ocean color data from SeaWiFS are used in this study to evaluate the realism of the modelled surface chlorophyll concentrations (considered as a proxy of phytoplankton biomass). When compared to *in situ* data in the Mediterranean Sea, the four-channel algorithm used by NASA to derive the oceanic chlorophyll concentration from ocean colour images from SeaWiFS performs poorly (Gregg and Casey, 2004). These low performances can be attributable to the presence of inorganic suspended matter causing overestimation of chlorophyll concentrations by global algorithms (Volpe et al., 2007). Therefore, in this study, we have chosen to utilize a five-channel algorithm (OC5) on 1.1-km resolution SeaWiFS data (Gohin et al., 2002). This algorithm with the ability to isolate the optical signal of chlorophyll pigment has been used successfully in the coastal ocean (Gohin et al., 2005), and particularly in the Mediterranean Sea (Fontana et al., 2009). The latter study shows a mean absolute error of 39.9% between *in situ* and satellite data. This error value is close -but however slightly lower- than those obtained in the studies of Lavigne et al. (2012) and Boss et al. (2008) for the NWMS. The thickness of the surface layer detected by SeaWiFS is called the first optical layer (Bricaud et al., 2010) and the lower limit of this layer depends of the amount of matter in the water column. In order to accurately compare the concentrations of the SeaWiFS-derived chlorophyll to those modelled, we must average the modelled concentrations of total chlorophyll (sum of chlorophyll concentrations of pico-, nano- and microphytoplankton) over the

first optical layer. The depth of this layer (z_{opt1}) is given by:

$$z_{opt1} = \frac{z_{eupho}}{\ln(100)} \quad (2)$$

where z_{eupho} is the depth of the modelled euphotic zone. The modelled total chlorophyll concentration averaged over the first optical layer is then calculated:

$$Chl_{opt1} = \frac{1}{z_{opt1}} \int_{h+\eta-z_{opt1}}^{h+\eta} Chl(z) dz \quad (3)$$

where h is the thickness of the water column, and η is the surface elevation.

2.3.2. Sea surface height data

The eddy kinetic energy deduced from the sea surface height anomaly is examined in order to confirm the presence of the eddy in 2001. Elevated levels of eddy kinetic energy indicate the presence and intensity of mesoscale dynamic structures. The eddy kinetic energy is deduced using weekly average geostrophic currents (zonal component U_{Aviso} , meridional component V_{Aviso}) provided by Aviso (Ducet et al., 2000). The average geostrophic current for the year 2001 ($\overline{U_{Aviso2001}}$, $\overline{V_{Aviso2001}}$) is subtracted from the weekly fields to obtain the geostrophic current anomaly (U'_{Aviso} , V'_{Aviso}). The weekly eddy kinetic energy (EKE_{Aviso}) is then calculated from the geostrophic current anomaly:

$$EKE_{Aviso} = \frac{1}{2} \left[(U'_{Aviso})^2 + (V'_{Aviso})^2 \right] \quad (4)$$

In order to make coherent comparisons with the satellite data, similar calculations are computed based on the model sea surface height output (η). Again, the yearly average sea surface height ($\overline{\eta}_{2001}$) is subtracted to retain the sea level anomaly only (η'). These modelled sea level anomalies (η') are interpolated in time (7 day moving average as used in the Optimal Interpolation altimetry treatment, refer to SSALTO/DUACS User Handbook) to

match up with the satellite-derived maps. The geostrophic current anomaly (U'_{Model}, V'_{Model}) is calculated using the thermal wind equation. The eddy kinetic energy of the model (EKE_{Model}) is given by:

$$EKE_{Model} = \frac{1}{2} \left[(U'_{Model})^2 + (V'_{Model})^2 \right] \quad (5)$$

2.4. ADCP data

A ship-mounted VMBB-150 kHz, merged at 3 m below the water surface, was used to measure the current velocity. Following Petrenko et al. (2005), the ADCP configuration used during the cruise was: 60 cells of 4 m depth, an ensemble average of 1 min and bottom tracking when possible. Consequently, the depth range of current data covers 11 to 243 m. The software for ADCP data analysis was provided by the French INSU (Institut National des Sciences de l'Univers) technical division.

3. Results

3.1. Detection of eddy presence in the study area in 2001

A series of seasonal short cruises (SARHYGOL: Regular and Automatic Survey of HYdrodynamics in the GoL) has been performed during the 2001 year every two months (Petrenko et al., 2005). We compared ADCP data from these cruises to the numerical results of realistic hydrodynamic model SYMPHONIE. In February 2001 (SARHYGOL 6), no eddy structure has been detected neither in the ADCP data nor in the model outputs in the NW part of the Gulf of Lion (data not shown). In late April-early May (SARHYGOL 7), the analysis of the ADCP data clearly shows the presence of an anticyclonic structure centred at $42^{\circ}38'N$ and $3^{\circ}12'E$ (Fig. 3) whose spatial extension and centre location are accurately reproduced by the hydrodynamic model (Fig. 3). In June (SARHYGOL 8), inertial oscillations complicate the local circulation and the presence of an anticyclonic eddy is

not retained (data not shown). Two other cruises (SARHYGOL 9 and 10, early September and early November, respectively) were planned but, due to bad meteorological conditions, no sampling in the study area could be performed.

In the physical model, an anticyclonic eddy has been detected by the technique of wavelet analysis (Doglioli et al., 2007) from July 17th to August 18th, 2001. In the Hu et al. (2011a)'s classification, since it lasts 32 days it is called a "long-life" coastal eddy. No field data were available in 2001 in the area to confirm its presence. However, the computation of kinetics energy from the Sea surface height enables us to validate its presence in the field. In Figure 4, the satellite-derived and modelled eddy kinetic energy (calculated as outlined in section 2.3.2) are compared. During the period in which wavelet analysis identifies the eddy, there is a clear signature of high eddy kinetic energy ($0.008 \text{ m}^2 \text{ s}^{-2}$) in the western Gulf of Lion (Figure 4-A). In the map of satellite-derived eddy kinetic energy, the values are equally elevated and shows a relatively good agreement with the model. The position of this high eddy kinetic energy patch is located slightly farther offshore and more to the South in the satellite derived map. It is however fundamental to bear in mind that the altimeters were designed to be used in the open ocean, and have difficulties in coastal regions due to contamination of the altimeter waveforms by land and inaccuracy of geophysical corrections (Bouffard et al., 2008). Despite the limitations of altimetry in the coastal domain, it has been successfully used to identify the presence of mesoscale activity in the Mediterranean Sea (Pascual et al., 2007).

By dividing the Gulf of Lion into eastern and western halves, the signal of this anticyclonic mesoscale eddy can be isolated. In a time-series of both eastern and western Gulf of Lion average eddy kinetic energy (Figure 4-B), there is a marked increase (from $0.001 - 0.002$ to $0.003 - 0.004 \text{ m}^2 \text{ s}^{-2}$) in energy in the western part of the gulf during the period in which the

eddy is present. This increase is well represented by the model. Indeed, the model (mean $0.0015 \pm 0.0011 \text{ m}^2 \text{ s}^{-2}$) reproduces the general trend of satellite-deduced (mean $0.0015 \pm 0.0011 \text{ m}^2 \text{ s}^{-2}$) eddy kinetic energy in the western Gulf of Lion ($r=0.747$, $p=1.4 \times 10^{-6}$, $n=30$) during the analysed time-series. The increased levels of satellite-deduced eddy kinetic energy in the western part of the Gulf of Lion confirm that the anticyclonic eddy detected in the physical model is actually present in the field. In this study we focus on this anticyclonic eddy and we hereafter refer to three particular dates corresponding to the beginning (A: July 23rd, 2001), middle (B: August 1st, 2001) and end (C: August 14th, 2001) of the eddy's lifetime. All the physical properties of the eddy are presented at these dates and at 20 m depth.

3.2. Physical Eddy Characteristics

The modelled temperature patterns show that the eddy (Fig. 5) has a distinct temperature signature of 20° to 21.5°C , slightly warmer than surrounding waters (18°C) and this trend tends to increase along its lifetime. According to the temperature field, the eddy is located along the Roussillon Coast and its location does not move much during its lifetime. However its size tends to increase with a clear motion of the eddy southwards at the end of the study period. The intensity of the modelled tangential velocity on the edge of the eddy ranges between 0.10 and 0.25 m s^{-1} . The current velocities are, most of time, higher on the western edge than on the eastern one. The modelled field of current velocity also shows that a northward coastal current along the Catalan Coast permanently feeds the eddy on its southwestern edge. The flow of the NC can be detected in the surrounding of the eddy and it is characterised by the southwestward high velocities (up to 0.3 m s^{-1}) on the southeast part of the study zone. It can be seen that the southeastern edge of the eddy is located close to the NC, especially at the end of its lifetime.

The vertical sections of temperature and current vertical velocities are presented in Figure 6. These sections begin south of the eddy at Cabo de Creus and pass through the centre of the eddy (defined as the maximum value of absolute relative vorticity). They clearly show a vertical structuring of the temperature distribution associated to the presence of the eddy. A few days after the eddy set up (date A), the eddy core displays a clear warming of the upper layer (down to 10 m). This warming is noticeable down to 40 m at the eddy centre, matching the maximum values of downwards velocities ($3 \times 10^{-4} \text{ m s}^{-1}$). On the contrary the southern and northern edges of the eddy show upwelling areas characterized by upwards velocities with maximum of $2 \times 10^{-4} \text{ m s}^{-1}$. It can be noted that the thermal front is more marked on the northern side of the eddy than on the southern one. At date B, the warming has continued (23°C at surface) and has spread at depth especially in the core of the eddy with temperatures higher than 20.5°C at 20 m depth. The pattern of vertical velocities has slightly changed. The area of upwelling delineating the northern edge of the eddy is still visible but the area of upwards velocities in the southern zone of study has almost vanished in the 0-40 m layer and it is then restricted to deeper layers. At date C, the surface temperatures in the eddy core have decreased by more than 1°C relative to those of date B but warming has propagated at depth ($\sim 20^\circ\text{C}$ at 40 m depth) suggesting a process of downwelling active until the end of the eddy's lifetime. Downwards vertical velocities which have entrained warmer surface waters down to 40 m depth are on the order of $2 \times 10^{-4} \text{ m s}^{-1}$. On the whole, the spatial pattern of vertical velocities has not much changed relative to the previous date. However, the area of upwards velocities observed at date B on the northern side of the eddy no longer reaches the surface layer at date C.

3.3. Nutrients and plankton distributions within and around the eddy

Figure 7 shows horizontal and vertical sections of nitrate concentrations at dates A, B, and C. The first snapshot (date A) reveals a decreasing surface gradient of nitrate from 1.6 mmol m^{-3} in the southern part of the transect to 0.7 mmol m^{-3} in the northern part (Fig. 7-A bottom). The eddy core corresponds to an area of minimum concentrations and it also displays the nitrate-depleted largest layer (Fig. 7-A top) spreading down the lower limit of the euphotic zone (around 40 m). The nitracline rises up from the eddy centre to its sides but the rising pattern is asymmetric. In agreement with the vertical velocities pattern (Fig. 6), the rising up of the nitracline is much more abrupt on the southern edge of the eddy than on the northern one. Deep concentrations of nitrate ($>2 \text{ mmol m}^{-3}$) largely penetrate into the euphotic layer up to 20 m depth south of the eddy. The horizontal field at 20 m (Fig. 7-A bottom) shows that the high nitrate concentrations spread over the coastal area located between Cabo de Creus and the southwestern edge of the eddy. Concentrations of nitrate are also high along the Roussillon Coast near the western side of the eddy suggesting that the process of nitrate rising up observed on the vertical pattern may extend northwards along the coast. At date B, the thickness of the nitrate-depleted layer has thinned with a general rising up of the nitracline on the transect (Fig. 7-B top). It can be noted however that the eddy's centre remains the area of nitrate lowest concentrations at both the surface and depth. Two enriched areas (1.3 mmol m^{-3}) between the nitracline and surface exactly match the edges of the eddy. The horizontal pattern at 20 m depth (Fig. 7-B bottom) show that this enriched-nitrate area spreads almost all around the eddy from the Cabo de Creus to half of its eastern edge. At date C, the depth and the shape of nitracline on the transect have not much changed relative to date B but the nitrate concentrations in the 0-20 m layer have globally increased up to a factor of 3 at some locations of the eddy (Fig. 7-C top). These locations

correspond to the two edges but also to its centre. On the horizontal section the area of high nitrate concentrations (2 mmol m^{-3} , Fig. 7-C bottom) is still present but its extension around the eddy is reduced relative to that of date B. This zone also tends to spread eastward to the eddy centre. The eddy core however still remains an area of minimum nitrate concentrations.

The modelled horizontal and vertical patterns of other nutrients (phosphate and silicate) are not shown in the present study because their distributions are very close to those of nitrate. The horizontal and vertical distributions of the abundance ratios of nitrate to phosphate (Fig. 8) and nitrate to silicate (Fig. 9) are presented hereafter because it will be demonstrated in the Discussion that these ratios have a strong influence on the type of phytoplankton growing in and around the eddy.

At the three dates, the nitrate:phosphate values display main changes in the 0-40 m layer varying from 22 to 100 (Fig. 8 top). Below the euphotic layer, the nitrate:phosphate values are around of 22, typical value for the Mediterranean deep waters (Mc Gill, 1969). Comparing the values obtained at the three dates, important changes can be seen. At date A, the area of highest ratios (around 60), indicating a phosphate deficit relative to nitrate, matches the eddy core but it also extends on the northern side of the eddy at shallower depths (Fig. 8-A top). The southern side of the eddy shows a sharp gradient of decreasing ratios southwards with values close to the typical deep waters ratios. As for the nitrate horizontal distributions, this area extends along the Roussillon and Languedoc Coasts near the western edge of the eddy (Fig. 8-A bottom). At date B, the nitrate:phosphate ratios have increased (up to 80) in the upper layer of the eddy especially in the southern part (Fig. 8-B top). The northeastern side of the eddy shows rather unchanged values (around 60) relative to those of date A within the 0-15 m layer. Below 15 m the ratios are close to 22. The low-ratio water mass present on the western side of the eddy at date A has progressed around the eddy (Fig. 8-B bottom).

This explains the low-ratio values at this place. The highest ratios (around 100) are found on the northern part of the transect eastwards. At date C, the nitrate:phosphate ratios have globally decreased over the eddy area (Fig. 8-C top). The eddy core and its southern side show maximum values of 55 while the northern part presents lower maximum values (around 45). The high ratio (>60) zone previously detected on the northern part of the study area (Fig. 8-C bottom) is still visible within the 0-20 m layer.

At the three dates the vertical gradient of the nitrate:silicate ratios (Fig. 9 top) is especially strong around the lower limit of the euphotic layer (40 m). The eddy core and, on the whole, the upper water column show ratios below 0.40 indicating a strong depletion of nitrate compared to silicate. These ratio values are typical of the end of the summer in the NWMS (Leblanc et al., 2003). It can be noted however that low ratios (0.45 to 0.65) are still found well below the lower limit of the euphotic layer (down to 70 m depth). At depth the ratio values increase and tend to approach the typical value observed in the deep waters of the western Mediterranean basin (Ribera d'Alcalà et al., 2003). The water mass upwelled near Cabo de Creus at date A shows rather high nitrate:silicate ratios (0.55) compared to those of the neighbouring areas (Fig. 9-A bottom). At dates B and C the area of high ratios at 20 m depth is located between the coast and all the western side of eddy (Fig. 9-B and 9-C bottom). Looking at the three spatial patterns may suggest that the upwelled water mass near Cabo de Creus (date A) could be merely entrained northwards along the coast (dates B and C) by the anticyclonic circulation induced by the eddy. But if another transect across the eddy is considered (*e.g.* that of nitrate concentrations, Fig. 10), it can be clearly seen that the upwelling of nutrients also occurs along the Roussillon and Languedoc Coasts and not only near the Cabo de Creus area. Hence the anticyclonic circulation entrains the water mass upwelled near Cabo de Creus northwards but the presence of the eddy also creates its own process

of upwelling along its western side.

The horizontal patterns of the modelled biomasses of phytoplankton groups at 20 m are presented in Figure 11 at the three dates A, B and C. On the whole the distributions of phytoplankton are spatially influenced by the presence of the eddy but the spatial structuring depends on the group considered. The distributions of micro- and nanophytoplankton are quite similar while those of picophytoplankton are distinct from the other ones at each of the analyzed dates. The eddy core generally shows a local maximum of picophytoplankton biomass ($0.15 \text{ mmol C m}^{-3}$, Fig. 11-3). If the whole studied zone is considered, the area of highest biomass corresponds to the NC flow. At date A, there is a continuity of high concentrations between the NC and the eddy core suggesting a possible seeding of the eddy by the NC at the beginning of the eddy's lifetime. The western and northern edges of the eddy are particularly depleted in picophytoplankton at the three dates. The northern part of its eastern side is also concerned by low biomasses at dates A and B. These very low concentrations are also found northeastwards along the Languedoc Coast. Both micro- and nanophytoplankton biomasses present minimum values ($<0.20 \text{ mmol C m}^{-3}$) within the eddy core during the studied period (Fig. 11-1 and 11-2). At date A, there is a clear asymmetry in the distributions of both groups around the eddy. While the western and northern edges show low biomasses of micro- and nanophytoplankton ($0.25 \text{ mmol C m}^{-3}$), 2-3 times higher biomasses are found on the eastern side. This high-biomass area is in spatial continuity with the high biomasses present at the northern coastal zone of the modelled domain (Fig. 11-A1 and 11-A2) suggesting at this time a coast-to-offshore transport of phytoplankton by the eddy. At date B, a significant increase in biomass of the micro- and nanophytoplankton (up to 0.40 and $0.60 \text{ mmol C m}^{-3}$, respectively) can be noted all along the western and northern sides of the eddy. This increase is especially marked on the northern edge (Fig. 11-B1 and 11-B2). On the contrary

the eastern edge of the eddy shows a moderate (resp. drastic) decrease in nanophytoplankton (resp. microphytoplankton) biomass compared to date A. At date C, the horizontal distributions of micro- and nanophytoplankton (Fig. 11-C1 and 11-C2) are again different from the ones at date B. The biomasses of the two groups have decreased along the western side of the eddy and returned to equivalent (resp. lesser) values than those of nanophytoplankton (resp. microphytoplankton) at date A. On the northern side of the eddy, the biomasses of nanophytoplankton have increased (to $0.8 \text{ mmol C m}^{-3}$, Fig. 11-C2) between dates B and C while those of microphytoplankton have remained constant (Fig. 11-C1). The eastern side of the eddy again displays high biomasses of the two groups but, at date C, this area of high biomasses extends all along this edge of the eddy (Fig. 11-C1 and 11-C2) and even well beyond its southward limit at date B.

The horizontal fields of the modelled biomasses of zooplankton groups at 20 m depth are shown in Figure 12. On the whole, as for phytoplankton groups the presence of the eddy in this area has clear effects on the distributions of the three groups of zooplankton. Here again the evolutions of the micro- and mesozooplankton groups are quite different than that of the nanozooplankton group. At the beginning of the eddy's lifetime (date A), the biomasses of the two largest-size classes are high (up to 0.25 and $1.75 \text{ mmol C m}^{-3}$, for meso- and microzooplankton resp.) within the eddy core while the biomasses are low on the southern and northern sides of the eddy (Fig. 12-A1 and 12-A2). The biomass levels in the eddy core do not really differ from those of the eastern and southern sides of the studied area. There is a spatial continuity of high biomasses between these external areas and the eddy core as it has been previously showed on the horizontal field of picophytoplankton at the same date (Fig. 11-A3). At date B, the biomasses of the two largest-size zooplankton groups have decreased around the eddy and neighbouring areas (Fig. 12-B1 and 12-B2). This decrease is especially

marked on the western side of the eddy for the microzooplankton group. On the contrary, the biomass values of these two groups remain at high levels (up to 0.25 and 1.40 mmol C m⁻³, for meso- and microzooplankton resp.) within the eddy core. At date C, the biomasses of microzooplankton and mesozooplankton (Fig. 12-C1 and 12-C2) do not change much within the eddy core compared to the previous snapshot. The changes rather occur on the sides of the eddy especially for the microzooplankton group. The biomasses of this group increase all around the eddy. While moderate on the western side of the eddy, the increase in microzooplankton biomass is marked (to 1.50 mmol C m⁻³) on the northeastern edge. Whatever the date considered, the nanozooplankton group shows the highest biomasses (up to 0.05 mmol C m⁻³, Fig. 12-3) in the area of the NC flow (Fig. 6). The other parts of the studied area -except the eddy one- are generally depleted in nanozooplankton with biomasses below 0.02 mmol C m⁻³. At date A, there is a decreasing gradient in the nanozooplankton biomasses between the NC area and the southwestern side of the eddy (Fig. 12-A3) suggesting that the northward current along the Catalan Coast may seed the eddy edge in this zooplankton group. At date B, the horizontal gradient between the NC and the southern part of the eddy still exists although it is less marked (Fig. 12-B3). The increase in the nanozooplankton biomass is remarkable (up to 0.03 mmol C m⁻³) almost all around the eddy's edges. At date C, the biomass levels have again decreased in the whole studied area (Fig. 12-C3). It is interesting to note however that biomasses still remain slightly higher (up to 0.025 mmol C m⁻³) than the background levels within the eddy core and also on its northeastern edge.

Vertical sections of several modelled plankton groups across the eddy are shown in Figure 13. The selected groups presented are those with the highest biomass levels (*e.g.* nanophytoplankton, microzooplankton) and those showing important development on the edges of the eddy (*e.g.* microphyto-

plankton, nanozooplankton). The model predicts the highest biomasses of phytoplankton on the edges of the eddy. The eastern side displays the highest concentrations whatever the considered date. This spatial structuring is especially manifest for microphytoplankton (Fig. 13-1). It is less evident for nanophytoplankton which is more distributed across the eddy, especially at dates B and C (Fig. 13-2). It can be further noted that the model shows, on the eastern edge of eddy, a vertical development depending on the considered phytoplankton group. Nanophytoplankton mainly blooms (up to $0.6 \text{ mmol C m}^{-3}$) within the upper layer (0-20 m) while microphytoplankton biomasses are found at their highest concentrations (up to $0.40 \text{ mmol C m}^{-3}$) below this layer (20-50 m depth). At dates B and C, the microphytoplankton maximum biomasses are located at the lower basis of the euphotic layer (Fig. 13-B1 and 13-C1). The distributions of the protist grazers (nano- and microzooplankton) mainly match those of nanophytoplankton. The maximum biomasses of these two groups are thus predicted within the upper layer 0-20 m and near the eastern edge of the eddy (Fig. 13-3 and 13-4) and this trend is increasingly marked the older the eddy. The high biomasses of nanozooplankton, previously seen at 20 m on the southwestern edge of the eddy (Fig. 12-A3 and 12-B3), clearly show a spatial extension between the Roussillon Coast and the eddy side at the beginning of the studied period (Fig. 13-A4 and 13-B4). In this area, the high biomasses extend down to the deeper part of the euphotic layer at date B. It is interesting to further note that the vertical distributions of protist grazers show a deepening of the iso-biomass lines in the core eddy. This shape matches those of the distributions of bacteria and picophytoplankton (data not shown) that are also grazed by both nanozooplankton and microzooplankton.

4. Discussion

4.1. Biogeochemical model evaluation

The set of available SeaWiFS images allows to evaluate the biogeochemical model in terms of representation of chlorophyll spatial patterns and concentrations during the study period. As such, the modelled concentrations of total chlorophyll are compared to the SeaWiFS-derived chlorophyll images (Fig. 14) in the studied area. On July 23th, 25th, 29th and August 5th, 2001, the SeaWiFS images clearly show a spatial structuring of surface chlorophyll concentrations due to the eddy presence in the study zone.

At the beginning (images of July 23th, 25th), the distributions of chlorophyll concentrations in the area of the eddy display strong patchiness. Firstly an enriched-chlorophyll area (>0.25 mg Chl m^{-3}) is visible near Cabo de Creus on the southern side of the eddy. An area of moderate concentrations (0.15-0.20 mg Chl m^{-3}) corresponding to the eddy core is found in the central part of the study area. In this zone chlorophyll concentrations are lower along the Roussillon Coast in the area corresponding to the western side of the eddy. Northwards along the Languedoc Coast an enriched-chlorophyll area (>0.30 mg Chl m^{-3}) is again observed. From this area a filament of high concentrations extends to the offshore domain delimiting the eastern edge of the eddy. This filament does not persist south of the $43^{\circ}N$. On July 29th and August 5th, 2001, the asymmetry in the spatial distributions of chlorophyll concentrations around the eddy area is still observed. Especially, the filament of higher chlorophyll concentrations on the eastern edge of the eddy remarkably persists until the end of the eddy's lifetime while on the western edge and in the central part of the eddy concentrations of chlorophyll are decreasing to very low values (<0.15 mg Chl m^{-3}). The position and the intensity of this filament do not show much changes until July 29th, even if the filament tends to be narrower and narrower. This filament is found more

to the Southwest on the satellite image of August, 5th and is characterized by a more spread-out shape and slightly lower concentrations.

Overall the model reproduces the patchy distributions observed at the beginning of the study sequence over the whole area as well as the more homogeneous distributions at the end. Maps of errors between the satellite-derived and modelled chlorophyll values confirm the correct performances of the model. The absolute percent differences range between 33 and 41% depending on the considered date (Fig. 14) and therefore fall most of time within the confidence interval of the satellite-derived values. The concentrations in the eddy core and along the western edge as well as their decreases over time are well predicted. The model also catches the presence of the high-chlorophyll filament during the eddy's lifetime. The modelled chlorophyll concentrations of the filament are however slightly underestimated except on the images of July 23th and August 5th. Whereas the model generally reproduces the high coastal concentrations (>0.30 mg Chl m^{-3}) along the Languedoc Coast, these concentrations decrease too quickly offshore in the filament. The position of the modelled filament is slightly shifted westward (~ 20 km) on July 23th and 25th. The position of the filament is better reproduced on July 30th and August 5th. It is interesting to note that the model is able to reproduce the change observed in the location of the filament between the last two dates.

The modelled contributions of the three phytoplankton groups to the total chlorophyll concentrations are in line with those of carbon biomasses (Fig. 11). The phytoplankton dominant groups in the filament (data not shown) are firstly nanophytoplankton and secondly microphytoplankton while chlorophyll biomass of picophytoplankton is very low. The contribution pattern is reversed in the eddy core for which total chlorophyll concentrations are low (<0.20 mg Chl m^{-3}) with a dominant contribution of the picophytoplankton group.

4.2. Impact of the eddy generation and functioning on the nutrients and plankton distributions

At date A, a strong upwelling of cold water is visible on the Languedoc Coast up to the subsurface layer (Fig. 5-A and 6-A top). This is a usual location of upwellings in this part of the Gulf of Lion (Millot, 1999). Its large horizontal extension clearly results from a strong northwest wind episode occurring several days before date A and participating to the eddy generation process (Hu et al., 2011a). According to this study, the northwesterly episode has to be persisting at least 75% of the previous three days to start the generation process. The wind induces an Ekman transport piling the water close to Cabo Creus. The sea level difference and the topography generate a northward current along the Roussillon Coast. If the vertical stratification is important, both circulations (Ekman transport and coastal jet) get linked generating an anticyclonic eddy. Later strong northwesterly can further fuel this eddy and maintain its existence over long periods, up to nearly two months as in the present study. The model shows that the initial upwelling of cold water has been associated to upwelling of nutrient-enriched waters especially north of Cap d'Agde (Fig. 7-A bottom). The phytoplankton community (mainly the largest-size groups) has already responded to this coastal enrichment in nutrients since high biomasses are found on the northern coast of Languedoc both in the model (Fig. 11) and the SeaWiFS images (23th July, Fig. 14). The upwelling zone does not extend southwest of Cap d'Agde and especially near the northern edge of the eddy where both nutrients and large-size phytoplankton concentrations remain low (Fig. 7-A bottom, 11-A1 and 11-A2).

At date A, the eddy acts, on its eastern edge, as a direct carrier of the high biomasses of the phytoplankton -produced several days before in the coastal zone- to the offshore domain (Fig. 11 and 14). This feature clearly explains the asymmetric vertical distributions predicted on the eddy transect at date

A (Fig. 13-A1 and 13-A2). The model also reveals two further features related to this coast-to-offshore transport at this time of the eddy's life: i) The transported biogenic matter does not reach the area of the NC and it is not be consequently exported beyond the shelf; ii) The transported matter is mainly composed of large-size phytoplankton and not of large zooplankton (Fig. 12-A1) which the generation time is much longer (Carlotti et al., 2007) than that of phytoplankton. The protist grazers with growth rates closer to those of phytoplankton (Le Quéré et al., 2005) show higher and higher biomasses (especially microzooplankton, Fig. 12-A2) southwards along the eastern edge of the eddy. The northward coastal current along the Roussillon Coast detected in the study of Hu et al. (2011a) is present at date A (Fig. 5-A) since the anticyclonic structure is already well established. Indeed as expected for an anticyclonic eddy (McGillicuddy et al., 1999) the studied eddy shows a downwelling process within its central part and an upwelling process on its edges (Fig. 6-A top). The consequences of these physical mechanisms on nutrients distributions are a deepening of nutriclines in the eddy core and a rising up of these nutriclines on the edges (Fig. 7-A top). Interestingly, although the upward velocities field appears to be less spread on the southern edge compared to the northern one, the nutrient concentrations in the euphotic layer are much higher at date A in the southern edge area of the eddy than in the northern one. This feature is explained by the existence of an upwelling zone north of Cabo de Creus (Fig. 5-A). The high-nutrient area extends along the Roussillon Coast probably through advection by the alongshore current coming from the Cabo de Creus region. North of Cap Leucate there are spots of nutrient-enriched waters (Fig. 7-A) suggesting some localized eddy-induced upwellings along the Roussillon Coast. The high nutrients concentrations at date B all along the western and northern edges of the eddy (Fig. 7-B bottom and 10) show that the processes of both advection from the south and eddy-induced upwelling intensify. The

shallowing of the depth and the proximity of the coast may explain why the rising up of nutrients is more intense on the western edge of the eddy than on its eastern side. Recent studies (Calado et al., 2010; Oke and Griffin, 2011) highlight that topographical forcing on coastal eddies favours occurrence of upwellings. The upwelling process brings high amounts of nutrients up to the surface on the western edge of the eddy while the eddy core displays lower concentrations all along the eddy's lifetime (Fig. 7-B bottom). The horizontal gradient of nutrient abundance is thus strong between the sides and the eddy's core but the abundance ratios between nutrients (nitrate, phosphate and silicate) also strongly change (Fig. 8-B bottom and 9-B bottom). Compared to the study zone (including the eddy core) the upwelled water on the coastal side of the eddy is enriched in nitrate relative to silicate as well in phosphate compared to nitrate. On the contrary, the water mass trapped inside the eddy core rather shows a strong deficit in phosphate relative to nitrate as the ratios modelled in the northeastern part of the study zone. High nitrate to phosphate ratios are a specific feature of the Gulf of Lion shelf waters (Diaz et al., 2001; Leblanc et al., 2003) and more generally of the surface Mediterranean Sea in summer (Moutin et al., 2008). The ratios of abundance and amounts of nutrients in the upwelled water on the western side of the eddy are typical of the end of the winter period (Leblanc et al., 2003; Charles et al., 2005) in the area. Thus, according to the model results, the occurrence of long-life anticyclonic eddies in the western zone of Gulf of Lion enables to create and maintain, along the Roussillon Coast and during several summer weeks, a nutrient availability typical of a winter period.

Although there is an abundance of nutrients on the western side of the eddy, the phytoplankton development remains low (dates A and C) or moderate (date B) in this area (Fig. 11 and 13). The highest biomasses, composed of the largest-size phytoplankton, are predicted on the northern side of the eddy at dates B and C. These spatial and temporal patterns are typical of

phytoplankton response to an upwelling event. The advection of water mass with cold temperatures prevent an immediate development of phytoplankton and the response of large-size phytoplankton to nutrient injection is on the order of three days (Wilkerson et al., 2006). In the present study the model predicts that the zone of maximal development for phytoplankton is the northern side of the eddy about two weeks following its generation. The eddy functioning thus enables the significant development of large phytoplankton types that are not usually present in such high concentrations at the surface during late summer in the NWMS (Leblanc et al., 2003; Marty et al., 2008). On the western and northern sides of the eddy every zooplankton groups remain at low levels all along the eddy's lifetime. This feature suggests that, in these areas of the eddy, the phytoplankton development is mainly controlled by bottom-up (nutrient availability) and physical (advection and temperature) processes. From date B, the high biomasses of phytoplankton blooming on the northern side are advected around the eddy and probably merge with plankton biomasses coming from the coastal upwelling still occurring on the Languedoc Coast. From this date, the filament visible both on the satellite images and the model outputs on the eastern side of eddy would then be composed of biogenic matter of two different sources. This aggregation process may explain why the highest biomasses of nanophytoplankton especially are predicted on the eastern side of the eddy at the surface from date B (Fig. 13-2) whereas nutrient availability is generally lower on this side of eddy (Fig. 7 and 10). At this time the persistence of nanophytoplankton over microphytoplankton in the filament at the surface, *i.e.* far from the upwelling source, corroborates some previous observations made on other upwelling systems (Fernandez and Bode, 1994; Botas et al., 1990). The model also shows, below the surface filament, the dominance and persistence of a microphytoplankton deep maximum all along the eddy's lifetime (Fig. 13-1). This deep maximum located around 40 m depth may

be directly attributable to the rising up of the nutricline on the eastern edge of the eddy. The depth of the microphytoplankton maximum at this year period in NWMS is usually higher and located between 60 and 80 m (Marty et al., 2008; Lasternas et al., 2011). At date A, the maximum of microphytoplankton biomass predicted at the surface, in addition to the deep one, may come from the plankton produced by the upwelling of the Languedoc Coast and transported by the eddy as proposed above. The eddy core shows a modelled dynamics of plankton ecosystem functioning very different from that described for the eddy sides. The smallest-size phytoplankton groups dominate in carbon biomasses (Fig. 11-3) and the concentrations of total surface chlorophyll are low all along the eddy lifetime (Fig. 14). Considering the nutrient pattern described above, the phytoplankton community structure of the eddy core makes of this part of the eddy a Low Phosphate Low Chlorophyll (LPLC, Moutin et al., 2008) system similar to the most oligotrophic areas of the Mediterranean Sea during summer (Mauriac et al., 2011). Biomasses of the three modelled groups of zooplankton are high in the eddy core (Fig. 12, 13-3 and 13-4) especially compared to its western side. These high biomasses are present from the beginning of the eddy's lifetime, suggesting a process of trapping and aggregation during the eddy generation. In details, the distributions of the smallest-size zooplankton appear to be, most of time, anti-correlated to those of the smallest-size phytoplankton suggesting a tight control by top-down processes (*e.g.* grazing). These patterns corroborate summer observational features in this area (Agawin et al., 2004; Charles et al., 2005). If converted in volumetric abundance (individuals per cubic meter) using the weight range of the two main species of copepods adults (0.02-0.04 mgC ind⁻¹, Razouls and Razouls, 1976) observed in the area, the carbon biomass of mesozooplankton inside the eddy ranges between 140 to 70 ind m⁻³ from dates A to C. Using the same conversion factor, the mesozooplankton modelled carbon biomass outside of the eddy

give some abundances ranging between 40 and 170 ind m⁻³. All these values fall in the range of abundances of the two main groups of mesozooplankton observed in the Northwestern Mediterranean Sea at the end of summer (Molinero et al., 2005; Mazzocchi et al., 2007).

Another intriguing feature of the eddy functioning is the spatial limit of the surface phytoplankton filament south of 43°N as observed on the SeaWiFS images and simulated by the model (Fig. 14). As there is a correct correspondence between the model outputs and observations, the model can be used to propose some assumptions to explain this feature. The presence of high biomasses of micro- and nanophytoplankton on the eastern edge of the eddy at the surface involves the development of the grazers throughout the eddy's life on this eddy side (Fig. 13-3 and 13-4). Contrary to those of the phytoplankton groups, distributions of all groups of zooplankton show persistence of high biomasses farther south than 43°N and sometimes joining the NC flow (Fig. 12). This model result suggests that the abrupt end of the chlorophyll filament may be due to top-down processes through grazing also explaining the sole persistence of zooplankton south of 43°N. The high biomasses of microphytoplankton persisting at depth due to the upwelled nutrients on the eddy side (Fig. 13-1), probably escape the predation process since there is no corresponding deep maxima of zooplankton. This model result suggests that the filament is only absent at the surface beyond the latitudinal limit of 43°N but persists at depth.

5. Conclusion and perspectives

This anticyclonic coastal eddy has some biogeochemical characteristics of anticyclonic eddies observed in the open ocean (McGillicuddy et al., 1999) as, for example, the low productivity at their core and rising up of nutrient on their edges. But the functioning and consequences of such coastal eddy in the NWMS are complicated by potential interactions with topog-

raphy, wind-induced upwelling along the Languedoc Coast and the nearby NC. Especially the proximity of the southern edge of the eddy with the NC makes possible the exchanges of organic matter (*i.e.* plankton) at times of the eddy's life as suggested by the model results. In the present study the coastal eddy contributes to the transport of organic matter from the coastal zone to the offshore domain and this is a common feature of coastal eddies recently showed in others systems (*e.g.* Dietze et al., 2009). The model results also show the importance of offshore-to-coastal transport, via seeding of the eddy with plankton at the beginning of its life.

The overall results of the model enable us to propose a schematic biogeochemical functioning of coastal eddies all along their lifetime in the western part of the Gulf of Lion (Fig. 15). As proposed by Hu et al. (2011a) this type of anticyclonic eddies needs two conditions to be generated: a persistent and strong northwestern wind and a strong stratification of the water column. The strong and persistent wind drives an intense upwelling along the northern Languedoc Coast. These upwellings enables the rising up to the surface of large amounts of nutrient that induce strong development of large-size phytoplankton several days later (Fig. 15-1). As the wind continues to blow the anticyclonic eddy sets up (Hu et al., 2011a) and the around-eddy advection allows the transport of the wind-induced phytoplankton coastal bloom offshore. At the same time the eddy shows upward vertical velocities on its edges creating upwelling of enriched nutrient waters. This process of eddy-induced upwelling is notably enhanced on the western edge of the eddy along the Roussillon Coast likely due to the shelf topography. In this coastal band, the upwelled water with nutrients characteristics close to that of deep water (high phosphate and high nitrate) allows the supply of large amounts of nutrients within the euphotic layer and even to the surface. On the contrary the core of the eddy displays a very different trophic status with clear deepening of the nutricline and a strong deficit in phosphate relative

to the other nutrients. This situation characterises the beginning of eddy's life around date A (Fig. 15-2). The around-eddy advection and relative lower temperatures of the upwelled water do not allow the large development of phytoplankton along the Roussillon Coast and this development is predicted to be high at the middle of the eddy's lifetime mainly in an area located between the northern Roussillon Coast (north of Cap Leucate) and the northern side of the eddy. The eddy-induced and wind-induced blooms of phytoplankton merge on the eastern side by advection and this process may thus explain the persistent occurrence of a filament of high chlorophyll observed on the offshore edge of the eddy all along the study period. Meanwhile the core of the eddy displays development of an active microbial loop based on smallest-size plankton groups (bacteria, picophytoplankton, nano- and microzooplankton). In this environment typical of the Mediterranean surface waters during the summer, the development of nano-, picoplankton and bacteria remains always low being both top-down controlled by the protist grazers trapped within the eddy core from its generation and bottom-up controlled by the low availability of nutrients (especially phosphate) (Fig. 15-3).

The model results show that changes in the plankton composition during the coast-to-offshore transport by around-eddy advection may explain the disappearance of the observed high chlorophyll filament south of 43°N at the surface. Mainly composed of largest-size phytoplankton close to the upwelled nutrient sources (northern side of the eddy and the Languedoc Coast), the plankton community shows higher and higher biomasses of zooplankton gradually as it is advected offshore and also during the eddy's lifetime. The process of top-down control is thus enhanced along the eastern side of the eddy. This feature, combined with the progressive lack of nutrients resource, may drive the disappearance of the surface chlorophyll filament South of 43°N . A filament mainly composed of microphytoplankton persists at depth

beyond this limit by escaping the predation process and benefiting from the eddy-induced rising up of nutrients in the euphotic layer. The southward transport of organic matter by the around-eddy advection interacts at times with the nearby NC making possible the export of coastal organic matter to the offshore domain. This picture characterises the functioning of the eddy from the middle to the end of its life (Fig. 15-4).

It would be interesting in some future studies to quantify the net fluxes of organic matter and nutrients exchanged during interactions between such coastal eddies and the NC over both an eddy life time and seasonal or annual scales if several eddies occur on these scales. Another possibility would be to extend realistic numerical simulations to some other years to highlight the possible variability of biogeochemical functioning of this type of eddy as it has been recently showed for physical functioning in the work of Hu et al. (2011a). In the present study the plankton food web model has enabled us to formulate many hypothesis regarding the plankton distributions and trophic interactions between plankton functional types in line with the presence of the eddy. Future years will see the implementation of long-term observatories in Northwestern Mediterranean Sea such as the French MOOSE (Mediterranean Ocean Observing System on Environment, <http://www.insu.cnrs.fr/co/expeditions-et-campagnes/moose-Mediterranean-ocean-observing-system-on-environment>) program. These observatories will be dedicated to the acquisition of many types of data such as plankton size spectra and dominant taxa at high frequency that may help to validate hypothesis made with such plankton food web models.

6. Acknowledgements

We kindly thank Paolo Lazzari for the outputs from the OPATM-BFM model. We thank Météo France for the weather forcings and MFS for the physical open boundary forcings. The altimeter products used here were pro-

duced by Ssalto/Duacs and distributed by Aviso, with support from Cnes (<http://www.aviso.oceanobs.com/duacs/>). Special thanks to J. Bouffard for assistance with satellite data access and invaluable interpretation of results and to P. Recoules for help in ADCP-model comparisons. The LATEX project is supported by the programs LEFE/IDAO and LEFE/CYBER of the INSU-Institut National des Sciences de l'Univers and by the Region PACA-Provence Alpes Côte d'Azur. Rose Campbell's research is funded in the form of a CIFRE grant in partnership with the ACRI-ST company.

References

- Agawin, N., Duarte, C., Agustí, S., Vaqué, D., 2004. Effect of N:P ratios on response of Mediterranean picophytoplankton to experimental nutrient inputs. *Aquatic Microbial Ecology* 34, 57–67.
- Allou, A., Forget, P., Devenon, J.L., 2010. Submesoscale vortex structures at the entrance of the gulf of lions in the northwestern mediterranean sea. *Continental Shelf Research* 30, 724–732.
- Anderson, T.R., Pondaven, P., 2003. Non-redfield carbon and nitrogen cycling in the Sargasso Sea: pelagic imbalances and export flux. *Deep Sea Res. I* 50, 573–591.
- Auger, P.A., Diaz, F., Ulses, C., Estournel, C., Neveux, J., Joux, F., Pujopay, M., Naudin, J.J., 2011. Functioning of the planktonic ecosystem on the Gulf of Lions shelf (NW Mediterranean) during spring and its impact on the carbon deposition: a field data and 3-D modelling combined approach. *Biogeosciences* 8, 3231–3261.
- Babin, M., Morel, A., Claustre, H., Bricaud, A., Kolber, Z., Falkowski, P.G., 1996. Nitrogen- and irradiance-dependent variations of the maxi-

- mum quantum yield of carbon fixation in eutrophic, mesotrophic and oligotrophic marine systems. *Deep Sea Res. I* 43, 1241–1272.
- Baklouti, M., Chevalier, C., Bouvy, M., Corbin, D., Pagano, M., Troussellier, M., Arfi, R., 2011. A study of plankton dynamics under osmotic stress in an estuary (Senegal River) using a 3D mechanistic model. *Ecological Modelling* 222, 2704–2721.
- Baklouti, M., Diaz, F., Pinazo, C., Faure, V., Quéguiner, B., 2006a. Investigation of mechanistic formulations depicting phytoplankton dynamics for models of marine pelagic ecosystems and description of a new model. *Prog. Oceanogr.* 71, 1–33.
- Baklouti, M., Faure, V., Pawlowski, L., Sciandra, A., 2006b. Investigation and sensitivity analysis of a mechanistic phytoplankton model implemented in a new modular numerical tool (Eco3M) dedicated to biogeochemical modelling. *Prog. Oceanogr.* 71, 34–58.
- Banque Hydrologique de France, 2010. Online: <http://hydro.eaufrance.fr>.
- Bertilsson, S., Berglund, O., Karl, D., Chisholm, S., 2003. Elemental composition of marine *Prochlorococcus* and *Synechococcus*: Implications for the ecological stoichiometry of the sea. *Limnol. Oceanogr.* 48(5), 1721–1731.
- Bosc, E., Bricaud, A., Antoine, D., 2004. Seasonal and interannual variability in algal biomass and primary production in the Mediterranean Sea, as derived from 4 years of SeaWiFS observations. *Global Biogeochem. Cycles* 18, GB1005.
- Boss, E., Swift, D., Taylor, L., Brickley, P., Zaneveld, R., Riser, S., Perry, M., Strutton, P., 2008. Observations of pigment and particle distributions in the western north atlantic from an autonomous float and ocean color satellite. *Limnol. Oceanogr.* 53, 21122122.

- Botas, J., Fernandez, E., Bode, A., Anadon, R., 1990. A persistent upwelling off the Central Cantabrian Coast (Bay of Biscay). *Estuarine, Coastal and Shelf Science* 30, 185–199.
- Bouffard, J., Vignudelli, S., Cipollini, P., Menard, Y., 2008. Exploiting the potential of an improved multimission altimetric data set over the coastal ocean. *Geophys. Res. Lett.* 35, L10601.
- Bricaud, A., Babin, M., Claustre, H., Ras, J., Tièche, F., 2010. Light absorption properties and absorption budget of southeast pacific waters. *J. Geophys. Res.* 115, C08009.
- Calado, L., da Silveira, I., Gangopadhyay, A., de Castro, B., 2010. Eddy-induced upwelling off Cape São Tomé (22°S, Brazil). *Cont. Shelf Res.* 30, 1181–1188.
- Carlotti, F., Bonnet, D., Halsband-Lenk, C., 2007. Development and growth rates of *Centropages typicus*. *Progress in Oceanography* 72, 164–194.
- Charles, F., Lantoiné, F., Brugel, S., Chrétiennot-Dinet, M.J., Quiroga, I., Rivière, B., 2005. Seasonal survey of the phytoplankton biomass, composition and production in a littoral NW Mediterranean site, with special emphasis on the picoplanktonic contribution. *Estuarine, Coastal and Shelf Science* 65, 199–212.
- Christaki, U., Courties, C., Karayanni, H., Giannakourou, A., Maravelias, C., Kormas, K., Lebaron, P., 2002. Dynamic Characteristics of *Prochlorococcus* and *Synechococcus* Consumption by Bacterivorous Nanoflagellates. *Microb. Ecol.* 43, 341–352.
- Claustre, H., Babin, M., Merien, D., Ras, J., Prieur, L., Dallot, S., Prasil, O., Dousova, H., Moutin, T., 2005. Toward a taxon-specific parameterization

- of bio-optical models of primary production: A case study in the North Atlantic. *J. Geophys. Res.* 110, C07S12.
- Conley, D., 1997. Riverine contribution of biogenic silica to the oceanic silica budget. *Limnol. Oceanogr.* 42(4), 774–777.
- Davidson, K., Gurney, W., 1999. An investigation of non-steady-state algal growth. II. Mathematical modelling of co-nutrient-limited algal growth. *J. Plankt. Res.* 21(5), 839–858.
- Demarcq, H., Wald, L., 1984. Surface dynamics of the Rhône plume inferred from infrared imagery. *Oceanol. Acta* 7(2), 159–162.
- Diaz, F., Raimbault, P., Boudjellal, B., Garcia, N., Moutin, T., 2001. Early spring phosphorus limitation of primary productivity in a NW Mediterranean coastal zone (Gulf of Lions). *Mar. Ecol. Prog. Ser.* 211, 51–62.
- Diaz, F., Raimbault, P., Conan, P., 2000. Small-scale study of primary productivity during spring in a Mediterranean coastal area (Gulf of Lions). *Cont. Shelf Res.* 20, 975–996.
- Dietze, H., Matear, R., Moore, T., 2009. Nutrient supply to anticyclonic meso-scale eddies off western Australia estimated with artificial tracers released in a circulation model. *Deep Sea Res. I* 56, 1440–1448.
- Doglioli, A.M., Blanke, B., Speich, S., Lapeyre, G., 2007. Tracking coherent structures in a regional ocean model with wavelet analysis: Application to Cape Basin eddies. *J. Geophys. Res.* 112, C05043.
- Ducet, N., Le Traon, P.Y., Reverdin, G., 2000. Global high-resolution mapping of ocean circulation from topex/poseidon and ers-1 and -2. *J. Geophys. Res.* 105, 19477–19498.

- Dufau-Julliand, C., Marsaleix, P., Petrenko, A., Dekeyser, I., 2004. Three-dimensional modeling of the Gulf of Lion's hydrodynamics (northwest Mediterranean) during January 1999 (MOOGLI3 Experiment) and late winter 1999: Western Mediterranean Intermediate Water's (WIW's) formation and its cascading over the shelf break. *J. Geophys. Res.* 109, C11002.
- Durrieu de Madron, X., Radakovitch, O., Heussner, S., Loye-Pilot, M.D., Monaco, A., 1999. Role of the climatological and current variability on shelf-slope exchanges of particulate matter: Evidence from the Rhône continental margin (NW Mediterranean). *Deep Sea Res. I* 46, 1513–1538.
- Eccleston-Parry, J., Leadbeater, B., 1995. Regeneration of phosphorus and nitrogen by four species of heterotrophic nanoflagellates feeding on three nutritional states of a single bacterial strain. *Appl. Environ. Microbiol.* 61(3), 1033–1038.
- Eden, C., Dietze, H., 2009. Effects of mesoscale eddy/wind interactions on biological new production and eddy kinetic energy. *J. Geophys. Res.* 114, C05023.
- Eisenhauer, L., Carlotti, F., Baklouti, M., Diaz, F., 2009. Zooplankton population model coupled to a biogeochemical model of the North Western Mediterranean Sea ecosystem. *Ecol. Model.* 220, 2865 – 2876.
- Eppley, R., 1972. Temperature and phytoplankton growth in the Sea. *Fish. Bull.* 70, 1063–1085.
- Estournel, C., Durrieu de Madron, X., Marsaleix, P., Auclair, F., Julliand, C., Vehil, R., 2003. Observation and modeling of the winter coastal oceanic circulation in the Gulf of Lion under wind conditions influenced by the continental orography (FETCH experiment). *J. Geophys. Res.* 108, C38059.

- Fasham, M., Flynn, K., Pondaven, P., Anderson, T., Boyd, P., 2006. Development of a robust marine ecosystem model to predict the role of iron in biogeochemical cycles: A comparison of results for iron-replete and iron-limited areas, and the SOIREE iron-enrichment experiment. *Deep Sea Res. I* 53, 333–366.
- Fernandez, E., Bode, A., 1994. Succession of phytoplankton assemblages in relation to the hydrography in the southern Bay of Biscay: a multivariate approach. *Sarsia Marina* 58, 191–205.
- Flexas, M.M., Durrieu de Madron, X., Garcia, M.A., Canals, M., Arnau, P., 2002. Flow variability in the Gulf of Lions during the MATER HFF experiment (March-May 1997). *J. Mar. Sys.* 33-34, 197–214.
- Fontana, C., Grenz, C., Pinazo, C., Marsaleix, P., Diaz, F., 2009. Assimilation of SeaWiFS chlorophyll data into a 3D-coupled physical-biogeochemical model applied to a freshwater-influenced coastal zone. *Cont. Shelf Res.* 29, 1397–1409.
- Forget, P., André, G., 2007. Can satellite-derived chlorophyll imagery be used to trace surface dynamics in coastal zone? A case study in the Northwestern Mediterranean Sea. *Sensors* 7, 884–904.
- Forget, P., Broche, P., Naudin, J.J., 2001. Reflectance sensitivity to solid suspended sediment stratification in coastal water and inversion: A case study. *Remote Sens. Environ.* 77, 92–103.
- Forget, P., Ouillon, S., 1998. Surface suspended matter off the Rhône river mouth from visible satellite imagery. *Oceanol. Acta* 21, 739–749.
- Franks, P., Walstad, L., 1997. Phytoplankton patches at fronts: a model of formation and response to wind events. *J. Mar. Res.* 55(1), 1–29.

- Garreau, P., Garnier, V., Schaeffer, A., 2011. Eddy resolving modelling of the gulf of lions and catalan sea. *Ocean Dynamics* 61, 991–1003.
- Gaspar, P., Y.G., Lefevre, J., 1990. A Simple Eddy Kinetic Energy Model for Simulations of the Oceanic Vertical Mixing: Tests at Station Papa and Long-Term Upper Ocean Study Site. *J. Geophys. Res.* 95, 16179–16193.
- Geider, R.J., Macintyre, H.L., Graziano, L.M., McKay, R.M.L., 1998. Responses of the photosynthetic apparatus of *Dunaliella tertiolecta* (Chlorophyceae) to nitrogen and phosphorus limitation. *Eur. J. Phycol.* 33(4), 315–332.
- Geider, R.J., MacIntyre, H.L., Kana, T.M., 1997. Dynamic model of phytoplankton growth and acclimation: Responses of the balanced growth rate and the chlorophyll a:carbon ratio to light, nutrient-limitation and temperature. *Mar. Ecol. Prog. Ser.* 143(1-3), 187–200.
- Gohin, F., Druon, J.N., Lampert, L., 2002. A five channel chlorophyll concentration algorithm applied to SeaWiFS data processed by SeaDAS in coastal waters. *Int. J. Remote Sens.* 23, 1639–1661.
- Gohin, F., Loyer, S., Lunven, M., Labry, C., Froidefond, J.M., Delmas, D., Huret, M., Herbland, A., 2005. Satellite-derived parameters for biological modelling in coastal waters: Illustration over the eastern continental shelf of the Bay of Biscay. *Remote Sens. Environ.* 95, 29–46.
- Gorbunov, M., Kolber, Z., Falkowski, P., 1999. Measuring photosynthetic parameters in individual algal cells by Fast Repetition Rate fluorometry. *Photosynth. Res.* 62(2-3), 141–153.
- Gregg, W.W., Casey, N.W., 2004. Global and regional evaluation of the SeaWiFS chlorophyll data set. *Remote Sens. Environ.* 93, 463–479.

- Hansen, B., Wernberg-Møller, T., Wittrup, L., 1997. Particle grazing efficiency and specific growth efficiency of the rotifer *Brachionus plicatilis* (Muller). *J. Exp. Mar. Biol. Ecol.* 215, 217 – 233.
- Harrison, W., Harris, L., Irwin, B., 1996. The kinetics of nitrogen utilization in the oceanic mixed layer: Nitrate and ammonium interactions at nanomolar concentrations. *Limnol. Oceanogr.* 41(1), 16–32.
- Heldal, M., Scanlan, D.J., Norland, S., Thingstad, F., Mann, N.H., 2003. Elemental composition of single cells of various strains of marine *Prochlorococcus* and *Synechococcus* using X-ray microanalysis. *Limnol. Oceanogr.* 48(5), 1732–1743.
- Hirst, A., Bunker, A., 2003. Growth of marine planktonic copepods: Global rates and patterns in relation to chlorophyll a, temperature, and body weight. *Limnol. Oceanogr.* 48, 1988–2010.
- Hu, Z., Doglioli, A., Petrenko, A., Dekeyser, I., 2011a. Numerical study of eddy generation in the western part of the Gulf of Lion. *J. Geophys. Res.* 116, C12030.
- Hu, Z., Doglioli, A., Petrenko, A., Dekeyser, I., 2011b. Study of a mesoscale anticyclonic eddy in the western part of the Gulf of Lion. *Journal of Marine Systems* 88, 3–11.
- Hu, Z., Doglioli, A., Petrenko, A., Marsaleix, P., Dekeyser, I., 2009. Numerical simulations of eddies in the Gulf of Lion. *Ocean Model.* 28(4), 203–208.
- Kersalé, M., Petrenko, A., Doglioli, A., Dekeyser, I. & Nencioli, F., submitted. Physical characteristics and dynamics of the coastal latex09 eddy derived from in situ data and numerical modeling. *J. Geophys. Res.* .

- Lacroix, G., Grégoire, M., 2002. Revisited ecosystem model (MODECO-GeL) of the Ligurian Sea: seasonal and interannual variability due to atmospheric forcing. *J. Mar. Sys.* 37, 229–258.
- Laney, S., Letelier, R., Abbott, M., 2005. Parameterizing the natural fluorescence kinetics of *Thalassiosira weissflogii*. *Limnol. Oceanogr.* 50(5), 1499–1510.
- Lasternas, S., Tunin-Ley, A., Ibañez, F., Andersen, V., Pizat, M.D., Lemée, R., 2011. Short-term dynamics of microphytoplankton abundance and diversity in NW Mediterranean Sea during late summer conditions (DYNAPROC 2 cruise; 2004). *Biogeosciences* 8, 743–761.
- Lavigne, H., D’Ortenzio, F., Claustre, H., Poteau, A., 2012. Towards a merged satellite and in situ fluorescence ocean chlorophyll product. *Biogeosciences* 9, 2111–2125.
- Lazzari, P., Solidoro, C., Ibello, V., Salon, S., Teruzzi, A., Béranger, K., Colella, S., Crise, A., 2011. Seasonal and inter-annual variability of plankton chlorophyll and primary production in the Mediterranean Sea: a modelling approach. *Biogeosciences Discussions* 8, 5379–5422.
- Le Quéré, C., Harrison, S., Prentice, I., Buitenhuis, E., Aumont, O., Bopp, L., Claustre, H., Cotrim Da Cunha, L., Geider, R., Giraud, X., Klass, C., Kohfeld, K., Legendre, L., Manizza, M., Platt, T., Rivkin, R., Sathyendranath, S., Uitz, J., Watson, A., Wolf-Gladrow, D., 2005. Ecosystem dynamics based on plankton functional types for global ocean biogeochemistry models. *Glob. Change Biol.* 11, 2016–2040.
- Leblanc, K., Queguiner, B., Garcia, N., Rimmelin, P., Raimbault, P., 2003. Silicon cycle in the NW Mediterranean Sea: seasonal study of a coastal oligotrophic site. *Oceanol. Acta* 4, 339–355.

- Lefèvre, D., Minas, H., Minas, M., Robinson, C., Williams, P.L., Woodward, E., 1997. Review of gross community production, primary production, net community production and dark community respiration in the Gulf of Lions. *Deep Sea Res. II* 44 (3-4), 801–832.
- Lévy, M., 2003. Mesoscale variability of phytoplankton and of new production: Impact of the large-scale nutrient distribution. *J. Geophys. Res.* 108, C113358.
- Lévy, M., 2008. The modulation of biological production by oceanic mesoscale turbulence. *Lect. Notes Phys.* 744, 219–261.
- Liu, H., Dagg, M., 2003. Interactions between nutrients, phytoplankton growth, and micro- and mesozooplankton grazing in the plume of the Mississippi River. *Mar. Ecol. Prog. Ser.* 258, 31–42.
- Ludwig, W., Dumont, E., Meybeck, M., Heussner, S., 2009. River discharges of water and nutrients to the Mediterranean and Black Sea: Major drivers for ecosystem changes during past and future decades? *Prog. Oceanogr.* 80, 199–217.
- Makino, W., Cotner, J., Sterner, R., 2003. Are bacteria more like plants or animals? Growth rate and resource dependence of bacterial C:N:P stoichiometry. *Funct. Ecol.* 17, 121–130.
- Marsaleix, P., Auclair, F., Floor, J.W., Herrmann, M.J., Estournel, C., Pairaud, I., Ulses, C., 2008. Energy conservation issues in sigma-coordinate free-surface ocean models. *Ocean Model.* 20, 61–89.
- Martin, A.P., Pondaven, P., 2003. On estimates for the vertical nitrate flux due to eddy pumping. *J. Geophys. Res.* 108, 3359.
- Martin, A.P., Richards, K.J., 2001. Mechanisms for vertical nutrient transport within a North Atlantic mesoscale eddy. *Deep Sea Res. II* 48, 757–773.

- Marty, J.C., Garcia, N., Raimbault, P., 2008. Phytoplankton dynamics and primary production under late summer conditions in the NW Mediterranean Sea. *Deep Sea Res. I* 55, 1131–1149.
- Mauriac, R., Moutin, T., Baklouti, M., 2011. Accumulation of DOC in Low Phosphate Low Chlorophyll (LPLC) area: is it related to higher production under high N:P ratio? *Biogeosciences* 8, 933–950.
- Mazzocchi, M., Christou, E., Capua, I.D., Fernandez De Puelles, M., Fondammani, S., Molinero, J., Nival, P., Siokou-Frangou, I., 2007. Temporal variability of centropages typicus in the mediterranean sea over seasonal-to-decadal scales. *Progress in Oceanography* 72, 214–232.
- Mc Gill, D., 1969. A budget for dissolved salts in the Mediterranean Sea. *Cahiers Océanographiques* 21, 543–554.
- McGillicuddy, D.J., Johnson, R., Siegel, D.A., Michaels, A.F., Bates, N.R., Knap, A.H., 1999. Mesoscale variations of biogeochemical properties in the Sargasso Sea. *J. Geophys. Res.* 104, 13381–13394.
- McGillicuddy, D.J., Robinson, A.R., Siegel, D.A., Jannasch, H.W., Johnson, R., Dickey, T.D., McNeil, J., Michaels, A.F., Knap, A.H., 1998. Influence of mesoscale eddies on new production in the Sargasso Sea. *Nature* 394, 263–266.
- Millot, C., 1979. Wind induced upwellings in the Gulf of Lions. *Oceanol. Acta* 2, 261–274.
- Millot, C., 1982. Analysis of upwelling in the Gulf of Lions, in: Nihoul J. C. J. (Ed.), *Hydrodynamics of semi-enclosed seas: Proceedings of the 13th International Liège Colloquium on Ocean Hydrodynamics*. Elsevier Oceanogr. Ser.. Amsterdam, The Netherlands. volume 34, pp. 143–153.

- Millot, C., 1990. The Gulf of Lions hydrodynamics. *Cont. Shelf Res.* 10, 885–894.
- Millot, C., 1999. Circulation in the Western Mediterranean Sea. *J. Mar. Sys.* 20, 423–442.
- Minas, M., Minas, H., 1989. Primary production in the Gulf of Lions with considerations to the Rhone River input. *Water Poll. Res. Reports* 13, 112–125.
- Molinero, J., Ibanez, F., Souissi, S., Chifflet, M., Nival, P., 2005. Phenological changes in the northwestern mediterranean copepods *centropages typicus* and *temora stylifera* linked to climate forcing. *Oecologia* 145, 640–649.
- Moore, C.M., Suggett, D., Holligan, P.M., Sharples, J., Abraham, E.R., Lucas, M.I., Rippeth, T.P., Fisher, N.R., Simpson, J.H., Hydes, D.J., 2003. Physical controls on phytoplankton physiology and production at a shelf sea front: a fast repetition-rate fluorometer based field study. *Mar. Ecol. Prog. Ser.* 259, 29–45.
- Moore, J.K., Doney, S.C., Lindsay, K., 2004. Upper ocean ecosystem dynamics and iron cycling in a global three-dimensional model. *Global Biogeochem. Cycles* 18, GB4028–.
- Moore II, T.S., Matear, R.J., Marra, J., Clementson, L., 2007. Phytoplankton variability off the Western Australian Coast: Mesoscale eddies and their role in cross-shelf exchange. *Deep Sea Res. II* 54, 943–960.
- Moutin, T. and, K.D., Duhamel, S., Rimmelin, P., Raimbault, P., Van Mooy, B., Claustre, H., 2008. Phosphate availability and the ultimate control of new nitrogen input by nitrogen fixation in the tropical Pacific Ocean. *Biogeosciences* 5, 95–109.

- Moutin, T., Raimbault, P., Golterman, H., Coste, B., 1998. The input of nutrients by the Rhône river into the Mediterranean Sea : recent observations and comparison with earlier data. *Hydrobiologia* 373/374, 237–246.
- Nejstgaard, J., Gismervik, I., Solberg, P., 1997. Feeding and reproduction by *Calanus finmarchicus*, and microzooplankton grazing during mesocosm blooms of diatoms and the coccolithophore *Emiliana huxleyi*. *Mar. Ecol. Prog. Ser.* 147, 197–217.
- Nielsen, M., 1997. Growth, dark respiration and photosynthetic parameters of the coccolithophorid *emiliana huxleyi* (Prymnesiophyceae) acclimated to different day length-irradiance combinations. *J. Phycol.* 33, 818–822.
- Oke, P.R., Griffin, D.A., 2011. The cold-core eddy and strong upwelling off the coast of new south wales in early 2007. *Deep Sea Research II* 58(5), 574–591.
- Oliver, R.L., Whittington, J., Lorenz, Z., Webster, I.T., 2003. The influence of vertical mixing on the photoinhibition of variable chlorophyll a fluorescence and its inclusion in a model of phytoplankton photosynthesis. *J. Plankton Res.* 25, 1107–1129.
- Omta, A.W., Kooijman, B., Dijkstra, H., 2007. Influence of (sub)mesoscale eddies on the soft-tissue carbon pump. *J. Geophys. Res.* 112, C11009.
- Oschlies, A., 2002. Nutrient supply to the surface waters of the North Atlantic: A model study. *J. Geophys. Res.* 107, C000275.
- Oschlies, A., Garçon, V., 1998. Eddy-induced enhancement of primary production in a model of the North Atlantic Ocean. *Nature* 394, 266–269.
- Pascual, A., Pujol, M., Larnicol, G., Traon, P.L., Rio, M., 2007. Mesoscale mapping capabilities of multisatellite altimeter missions: First results with

- real data in the Mediterranean Sea. *Journal of Marine Systems* 65, 190 – 211.
- Petrenko, A., Leredde, Y., Marsaleix, P., 2005. Circulation in a stratified and wind-forced Gulf of Lions, NW Mediterranean Sea: *in situ* and modeling data. *Cont. Shelf Res.* 25, 7–27.
- Petrenko, A.A., 2003. Variability of circulation features in the Gulf of Lion NW Mediterranean Sea. Importance of inertial currents. *Oceanol. Acta* 26, 323–338.
- Putt, M., Stoecker, D., 1989. An experimentally determined carbon:volume ratio for marine "oligotrichous" ciliates from estuarine and coastal waters. *Limnol. Oceanogr.* 34(6), 1097–1103.
- Razouls, C., Razouls, S., 1976. Dimensions, poids sec, valeur calorifique et courbes de croissance de deux populations naturelles de coppodes planctoniques. *Vie et Milieu* 26B, 281–297.
- Reffray, G., Fraunié, P., Marsaleix, P., 2004. Secondary flows induced by wind forcing in the Rhône region of freshwater influence. *Ocean Dyn.* 54, 179–196.
- Ribera d'Alcalà, M., Civitarese, G., Conversano, F., Lavezza, R., 2003. Nutrient ratios and fluxes hint at overlooked processes in the Mediterranean Sea. *Journal of Geophysical Research* 108(C9), 7–1–7–16.
- Riegman, R., Stolte, W., Noordeloos, A., Slezak, D., 2000. Nutrient uptake and alkaline phosphatase (ec 3:1:3:1) activity of *emiliana huxleyi* (Prymnesiophyceae) during growth under N and P limitation in continuous cultures. *J. Phycol.* 36(1), 87–96.

- Rubio, A., Barnier, B., Jord, G., Espino, M., Marsaleix, P., 2009. Origin and dynamics of mesoscale eddies in the Catalan Sea (NW Mediterranean): Insight from a numerical model study. *J. Geophys. Res.* 114, C06009.
- Sammari, C., Millot, C., Prieur, L., 1995. Aspects of the seasonal and mesoscale variabilities of the Northern Current in the western Mediterranean Sea inferred from the PROLIG-2 and PROS-6 experiments. *Deep Sea Res. I* 42, 893–917.
- Sarthou, G., Timmermans, K., Blain, S., Tréguer, P., 2005. Growth physiology and fate of diatoms in the ocean: a review. *J. Sea Res.* 53, 25–42.
- Sasai, Y., Richards, K.J., Ishida, A., Sasaki, H., 2010. Effects of cyclonic mesoscale eddies on the marine ecosystem in the Kuroshio Extension region using an eddy-resolving coupled physical-biological model. *Ocean Dynamics* 60, 693–704.
- Sempéré, R., Charrière, B., Van Wambeke, F., Cauwet, G., 2000. Carbon inputs of the Rhône River to the Mediterranean Sea: Biogeochemical implications. *Global Biogeochem. Cycles* 14, 669–681.
- Siegel, D.A., McGillicuddy, D.J., Fields, E.A., 1999. Mesoscale eddies, satellite altimetry, and new production in the Sargasso Sea. *J. Geophys. Res.* 104, 13359–13379.
- Sterner, R., Robinson, J., 1994. Threshold for growth in *Daphnia magna* with high and low phosphorus diets. *Limnol. Oceanogr.* 39, 1228–1232.
- Suthers, I., Young, J., Baird, M., Roughan, M., Everett, J., Brassington, G., Byrne, M., Condie, S., Hartog, J., Hassler, C., Hobday, A., Holbrook, N., Malcolm, H., Oke, P., Thompson, P., Ridgway, K., 2011. The strengthening East Australian Current, its eddies and biological effects: an introduction and overview. *Deep Sea Research II* 58(5), 538–546.

- Sweeney, E.N., McGillicuddy, D.J., Buesseler, K.O., 2003. Biogeochemical impacts due to mesoscale eddy activity in the Sargasso Sea as measured at the Bermuda Atlantic Time-series Study (BATS). *Deep Sea Res. II* 50, 3017–3039.
- Thingstad, T., Skjoldal, E., et Bohne, R., 1993. Phosphorus cycling and algal-bacterial competition in Sandsfjord, western Norway. *Mar. Ecol. Prog. Ser.* 99(3), 239–259.
- Thornley, J., Cannell, M., 2000. Modelling the components of plant respiration: representation and realism. *Ann. Bot.* 85, 55–67.
- Timmermans, K., der Wagt, B.V., Veldhuis, M., Maatman, A., de Baar, H., 2005. Physiological responses of three species of marine pico-phytoplankton to ammonium, phosphate, iron and light limitation. *J. Sea Res.* 53(1-2), 109–120.
- Tintoré, J., Wang, D., La Violette, P., 1990. Eddies and Thermohaline Intrusions of the Shelf/Slope Front off the Northeast Spanish Coast. *J. Geophys. Res.* 95, 1627–1633.
- Tyrrell, T., Taylor, A., 1996. A modelling study of *Emiliana huxleyi* in the NE atlantic. *J. Marine Syst.* 9(1-2), 83–112.
- Ulses, C., Estournel, C., Durrieu de Madron, X., Palanques, A., 2008. Suspended sediment transport in the Gulf of Lions (NW Mediterranean): Impact of extreme storms and floods. *Cont. Shelf Res.* 28, 2048–2070.
- Urabe, J., Watanabe, Y., 1992. Possibility of N and P limitation for planktonic cladocerans: an experimental test. *Limnol. Oceanogr.* 37, 244–25.
- Vichi, M., Pinardi, N., Masina, S., 2007. A generalized model of pelagic biogeochemistry for the global ocean ecosystem. part i: Theory. *J. Mar.*

- Sys. 64, 89 – 109. Contributions from Advances in Marine Ecosystem Modelling Research, 27-29 June, 2005, Plymouth, UK, AMEMR.
- Vincent, D., Slawyk, G., L’Helguen, S., Sarthou, G., Gallinari, M., Seuront, L., Sautour, B., Ragueneau, O., 2007. Net and gross incorporation of nitrogen by marine copepods fed on ^{15}N -labelled diatoms: Methodology and trophic studies. *J. Exp. Mar. Biol. Ecol.* 352, 295–305.
- Volpe, G., Santoleri, R., Vellucci, V., Ribera d’Alcal, M., Marullo, S., D’Ortenzio, F., 2007. The colour of the Mediterranean Sea: Global versus regional bio-optical algorithms evaluation and implication for satellite chlorophyll estimates. *Remote Sens. Environ.* 107, 625–638.
- Vrede, K., Heldal, M., Norland, S., Bratbak, G., 2002. Elemental composition (C,N,P) and cell volume of exponentially growing and nutrient-limited bacterioplankton. *Appl. Environ. Microbiol.* 68(6), 2965–2971.
- Wilkerson, F.P., Lassiter, A., Dugdale, R., Marchi, A., Hogue, V., 2006. The phytoplankton bloom response to wind events and upwelled nutrients during the CoOP WEST study. *Deep Sea Res. II* 53, 3023–3048.

7. Figures

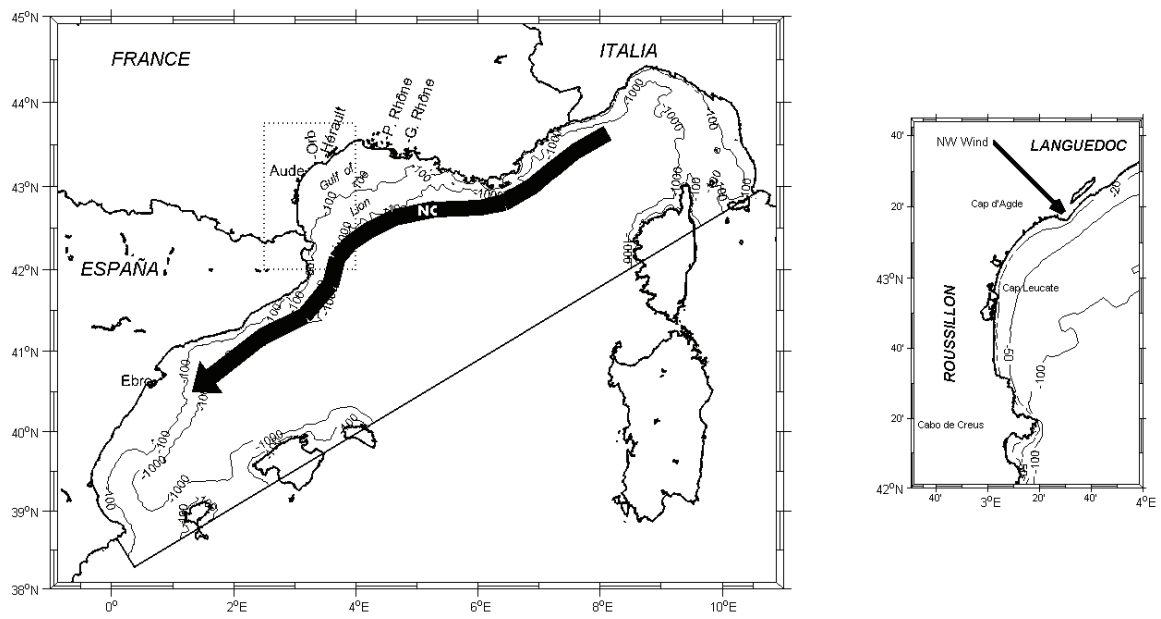


Figure 1: Model domain bathymetry and zoom on the study area. Arrow indicates the main flow of the Northern Current (NC). Rivers taken into account by the model are named. Isobaths at 50, 100 and 1000 m are shown in the modeled zone.

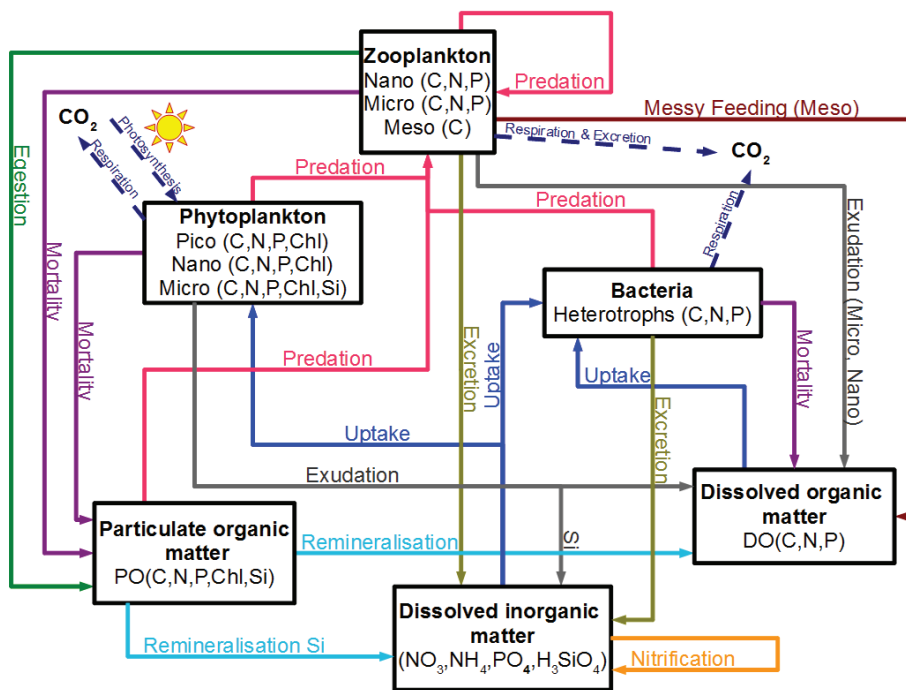


Figure 2: Model schematic diagram. See Method section for abbreviations.

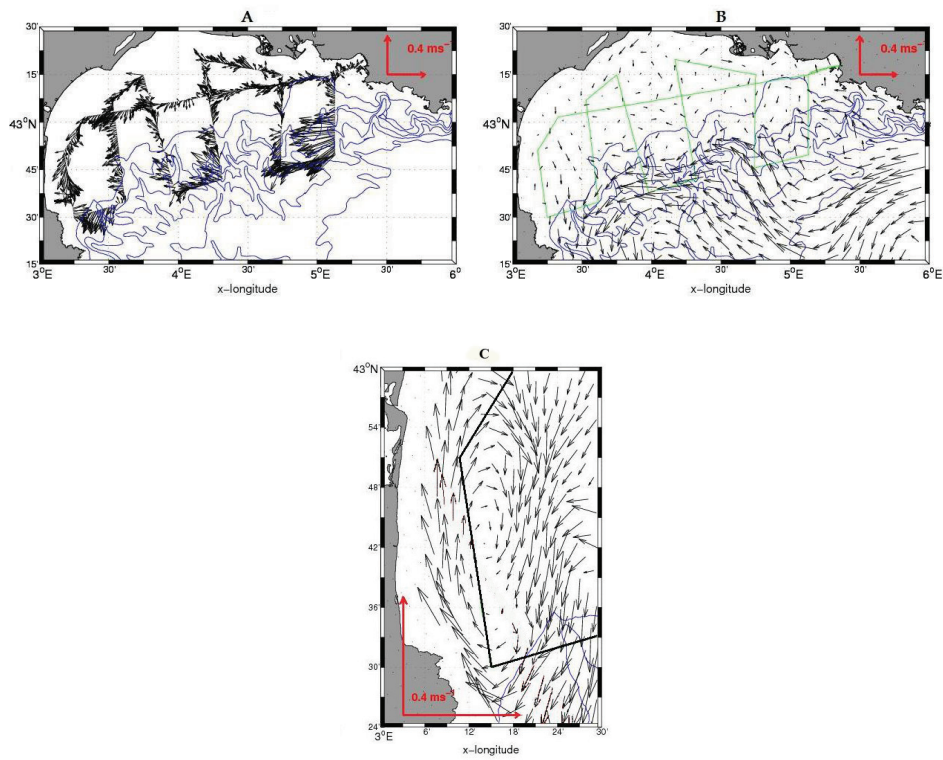
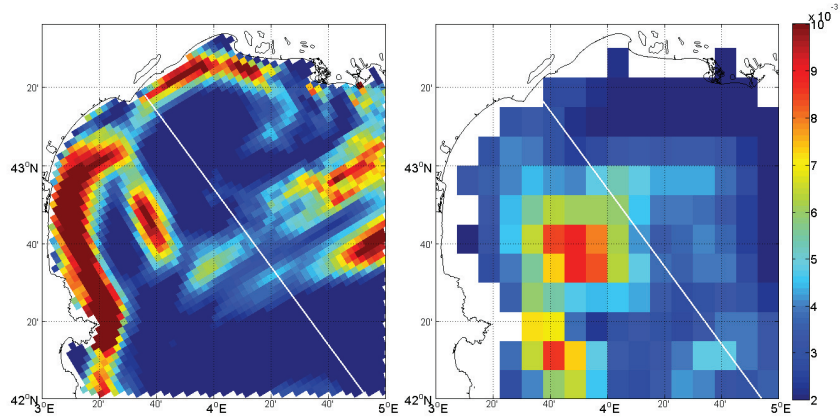
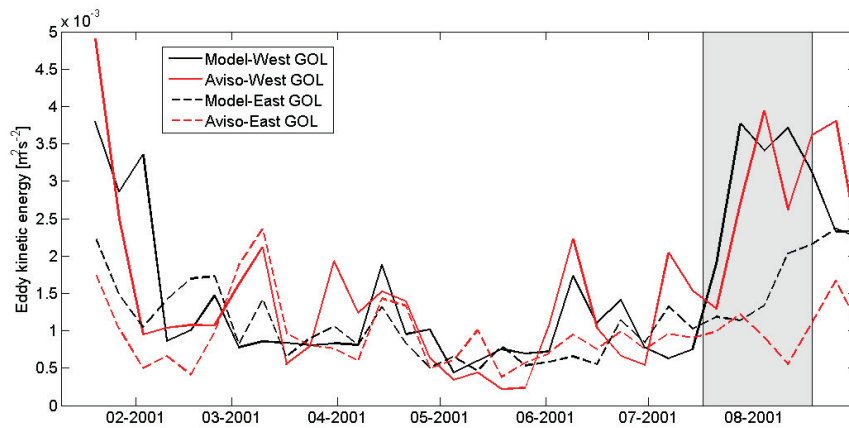


Figure 3: Comparisons between fields of ADCP current vectors (at 24 m) [A] and corresponding modelled current vectors [B] during the SARHYGOL 7 cruise (Early May 2001) in the Gulf of Lion. [C] Zoom of the modelled current vectors at 24 m in the NW part of the Gulf of Lion. Broken black (or green) lines show the cruise transects.



[A]



[B]

Figure 4: A) Average of modelled eddy kinetic energy [$in m^2 s^{-2}$] (left) and satellite-derived eddy kinetic energy (right) during the eddy's lifetime. White line indicates the separation of the gulf in eastern and western zones. B) Time-series of the spatially-averaged eddy kinetic energy in the western (lines) and eastern (dashed lines) parts of the Gulf of Lion. Red: values derived from the geostrophic currents provided by Aviso. Black: values derived from sea surface elevation of the model. The shaded grey area indicates the presence of the eddy as defined using wavelet analysis.

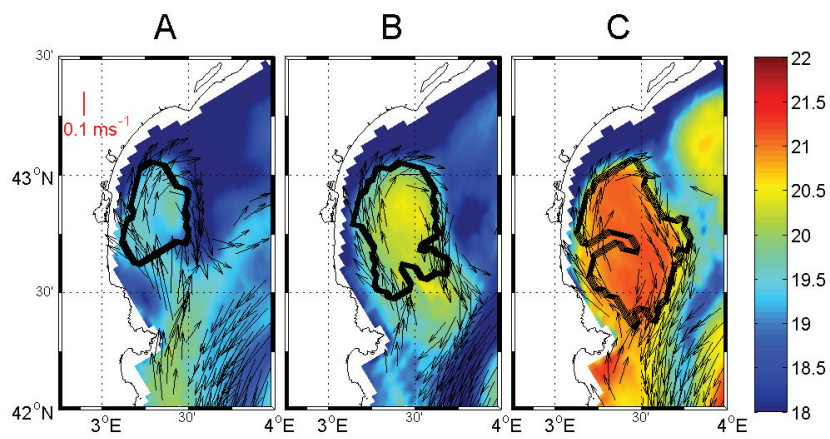


Figure 5: Fields of modelled temperature with wavelet analysis contour superimposed ($^{\circ}\text{C}$) at 20 m depth, at the beginning (A: July 23, 2001), middle (B: August 1, 2001) and end (C: August 15, 2001) of the eddy's lifetime. Vectors represent the current where the speed is greater than 0.1 m s^{-1} .

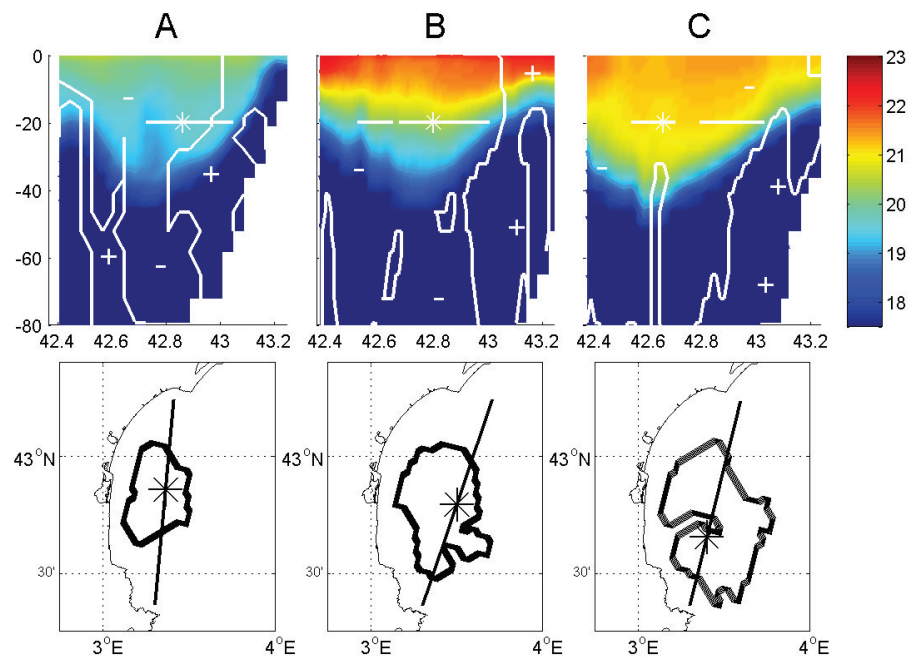


Figure 6: Top: Vertical sections of temperature ($^{\circ}\text{C}$) from Cap Creus (left) through the centre of the eddy (star) at the beginning (A: July 23, 2001), middle (B: August 1, 2001) and end (C: August 15, 2001) of the eddy's lifetime. The white horizontal line and star indicate the wavelet-analysis defined contour and centre of the eddy. The zero contour for vertical velocity is included: plus signs indicate upwards, minus signs indicate downwards. Bottom: The positions of section across the eddy and centre (black star) are indicated.

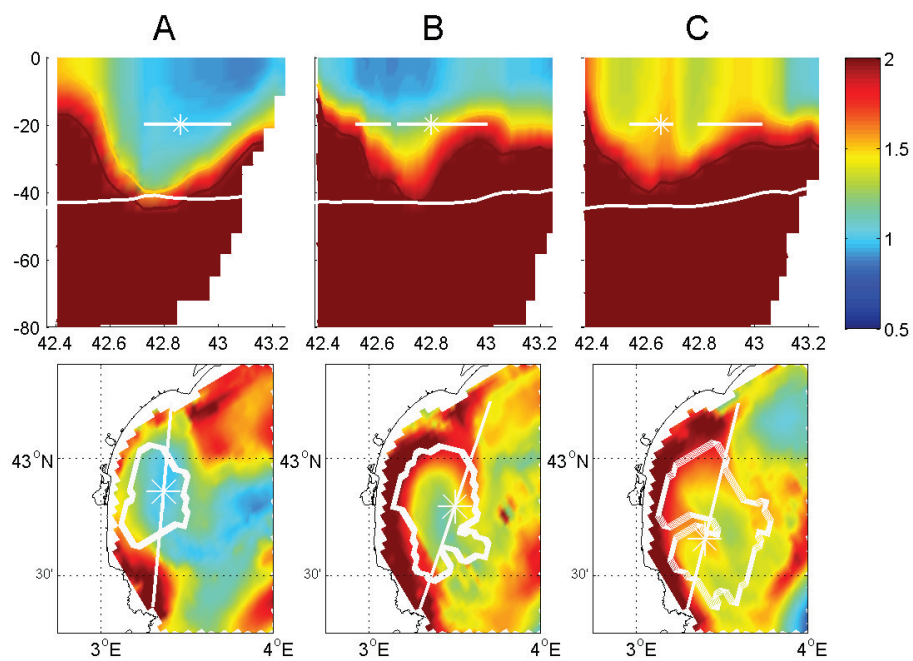


Figure 7: Top: Vertical sections of modelled nitrate concentrations (mmol m^{-3}) as indicated in bottom of this figure. The white horizontal line and star indicate the wavelet-analysis defined contour and centre of eddy. The continuous white line corresponds to the lower limit of the euphotic layer. Bottom: Horizontal fields of nitrate concentrations at 20 m depth, at the beginning (A: July 23, 2001), middle (B: August 1, 2001) and end (C: August 15, 2001) of the eddy's lifetime.

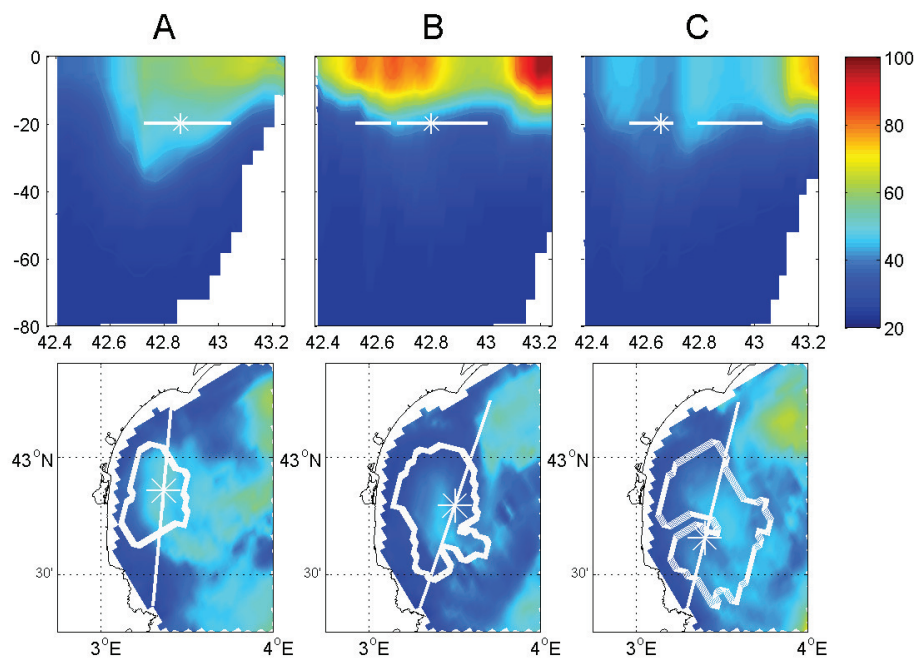


Figure 8: Top: Vertical sections of modelled nitrate:phosphate (mol/mol) as indicated in bottom of this figure. The white horizontal line and star indicate the wavelet-analysis defined contour and centre of eddy. Bottom: Ratios of nitrate to phosphate at 20 m depth, at the beginning (A: July 23, 2001), middle (B: August 1, 2001) and end (C: August 15, 2001) of the eddy's lifetime.

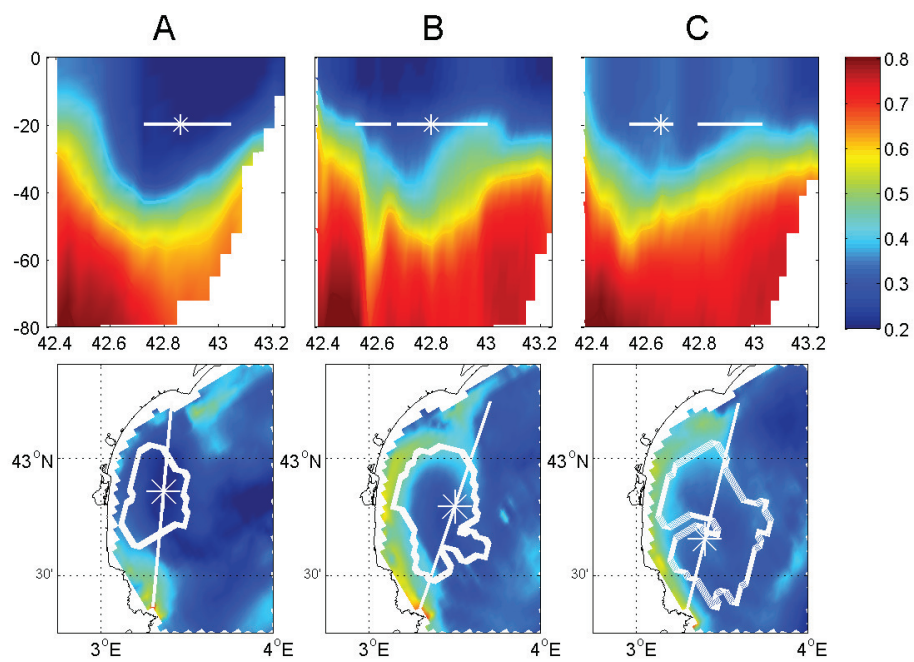


Figure 9: Top: Vertical sections of modelled nitrate:silicate as indicated in bottom of this figure. The white horizontal line and star indicate the wavelet-analysis defined contour and centre of eddy. Bottom: Ratios of nitrate to silicate at 20 m depth, at the beginning (A: July 23, 2001), middle (B: August 1, 2001) and end (C: August 15, 2001) of the eddy's lifetime.

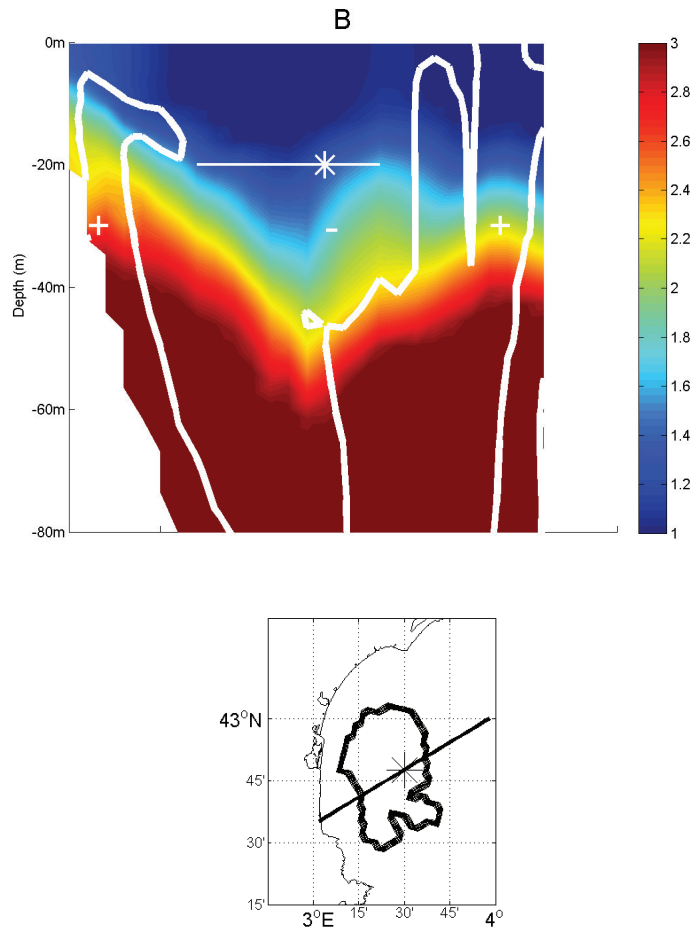


Figure 10: Top: Vertical section of nitrate (mmol m^{-3}) across the eddy at date B (August 1, 2001). The zero contour for vertical velocity is included: plus signs indicate upwards velocities, minus signs indicate downwards velocities. The white horizontal line and star indicate the wavelet-analysis defined contour and centre of the eddy. Bottom: The position of the section across the eddy and centre (black star) are indicated.

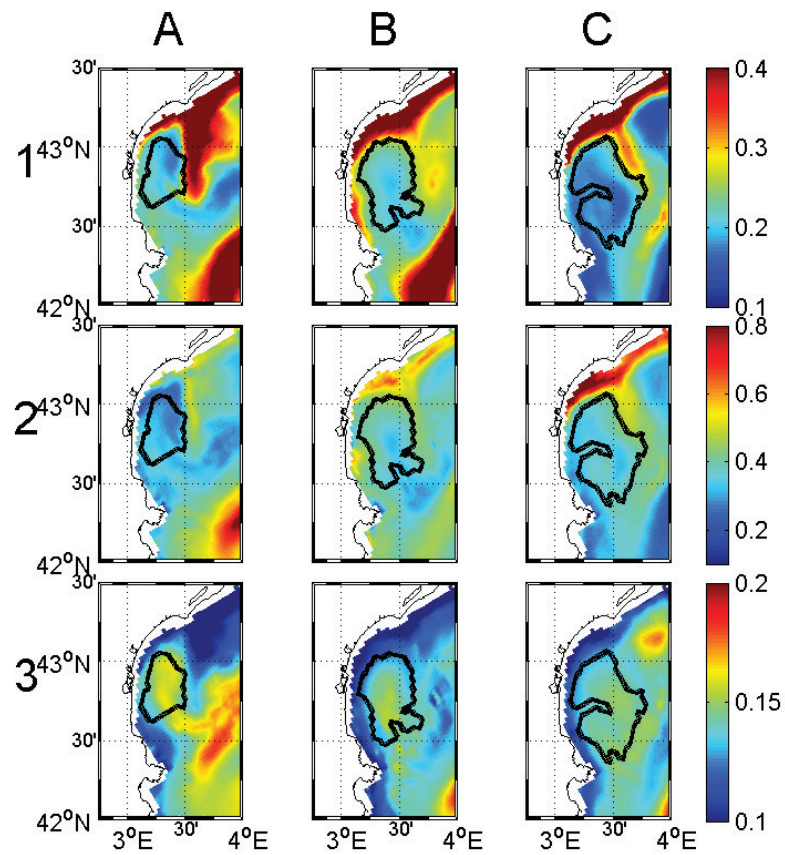


Figure 11: Horizontal fields of phytoplankton functional types groups (mmol C m^{-3}) with wavelet analysis contour superimposed at 20 m depth, at the beginning (A: July 23, 2001), middle (B: August 1, 2001) and end (C: August 15, 2001) of the eddy's lifetime. 1. Microphytoplankton. 2. Nanophytoplankton. 3. Picophytoplankton.

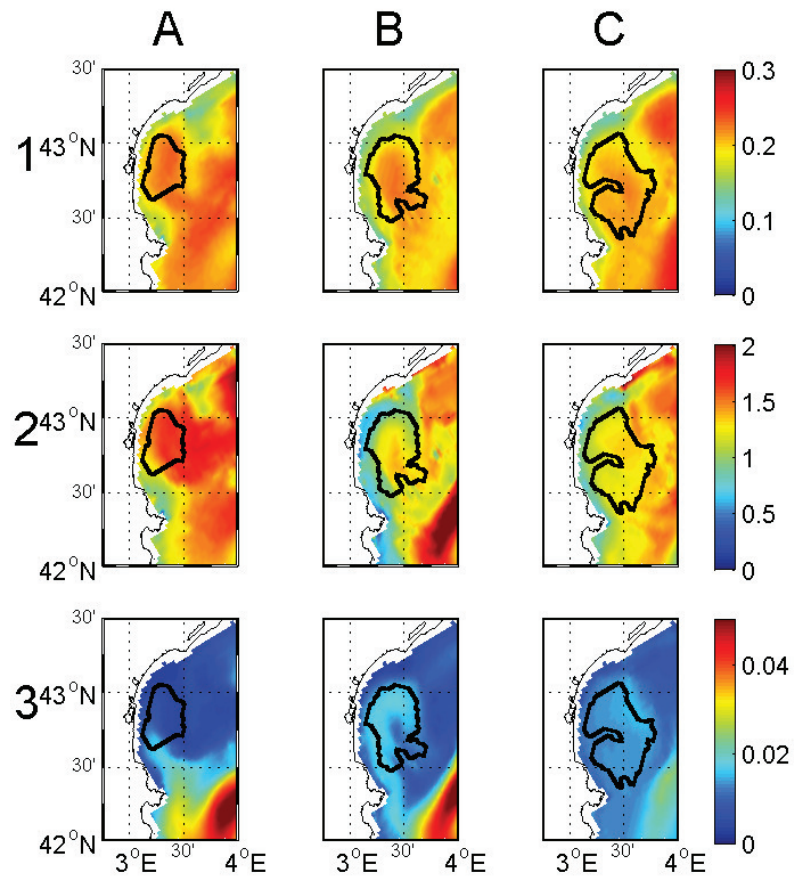


Figure 12: Horizontal fields of zooplankton functional types groups (mmol C m^{-3}) with wavelet analysis contour superimposed at 20 m depth, at the beginning (A: July 23, 2001), middle (B: August 1, 2001) and end (C: August 15, 2001) of the eddy's lifetime. 1. Mesozooplankton. 2. Microzooplankton. 3. Nanozooplankton.

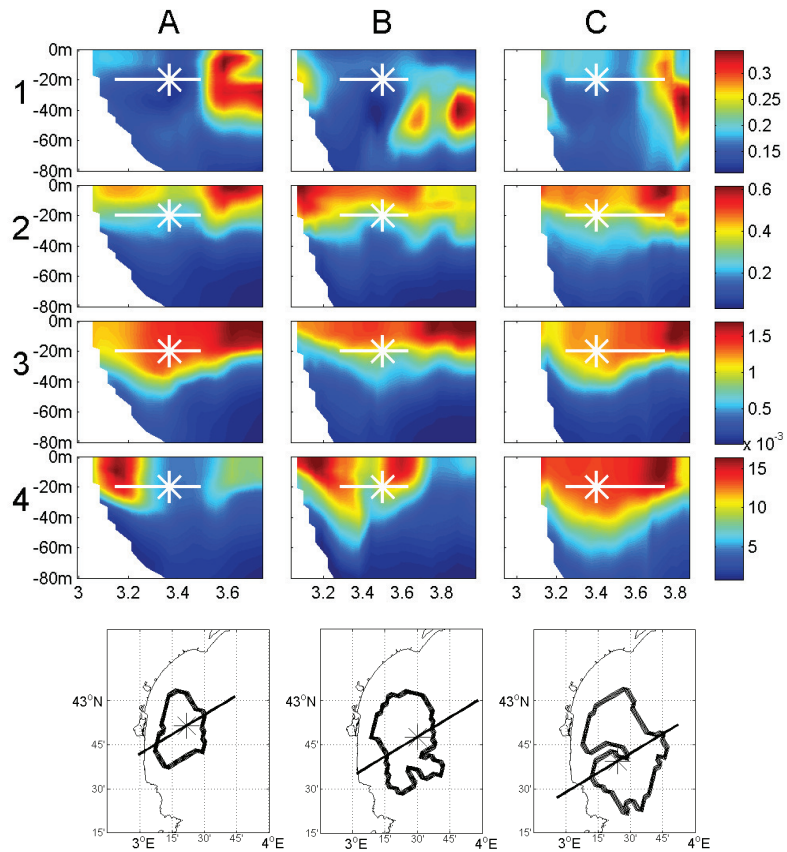


Figure 13: Top: Vertical sections of plankton functional types groups (mmol C m^{-3}) going east-west across the eddy at the beginning (A: July 23, 2001), middle (B: August 1, 2001) and end (C: August 15, 2001) of the eddy's lifetime. The white horizontal line and star indicate the wavelet-analysis defined contour and centre of the eddy. 1. Microphytoplankton. 2. Nanophytoplankton. 3. Microzooplankton. 4. Nanozooplankton. Bottom: The positions of the section across the eddy and centre (black star) are indicated.

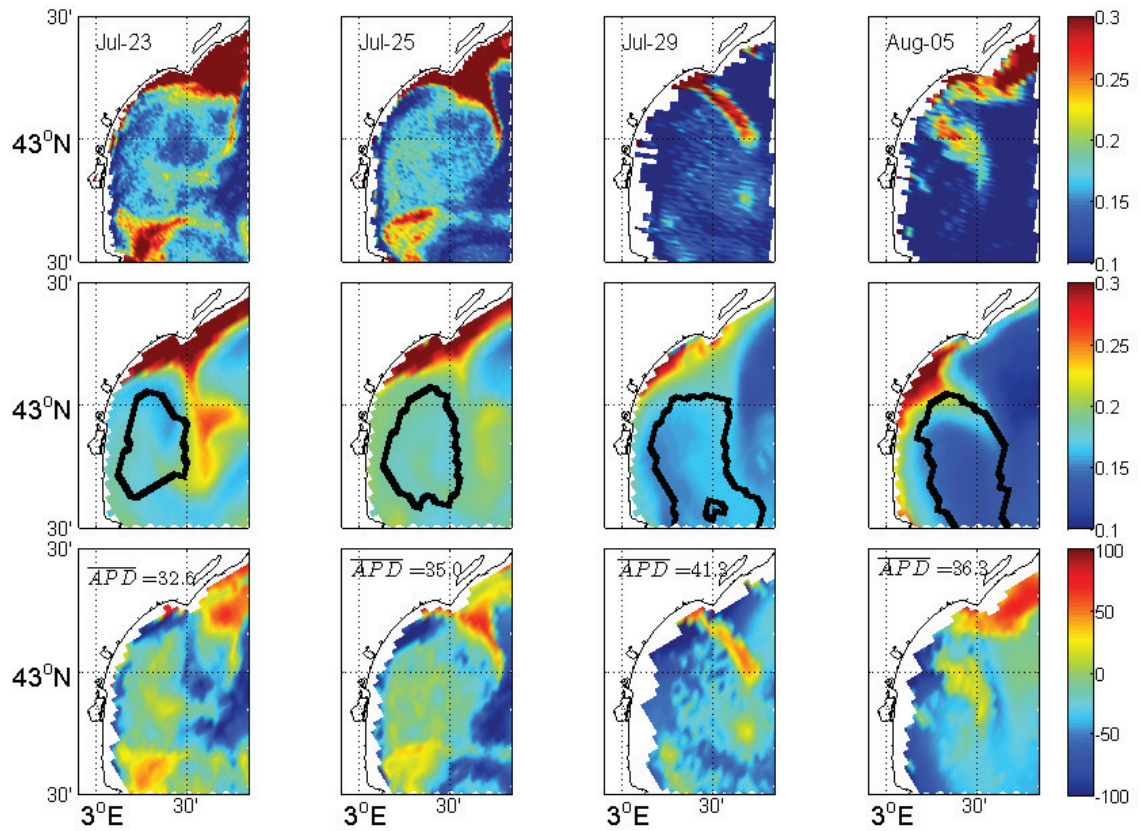


Figure 14: Chlorophyll concentrations (mg Chl m^{-3}) derived from SeaWiFS using OC5 (upper), modelled total chlorophyll concentrations within the first optical layer (middle) and the absolute percent difference (APD) between satellite and modelled values (lower) on July 23rd, July 25th, July 29th, and August 5th 2001. The wavelet analysis contours are superimposed on the model outputs. The mean APD (\overline{APD}) for each date is included.

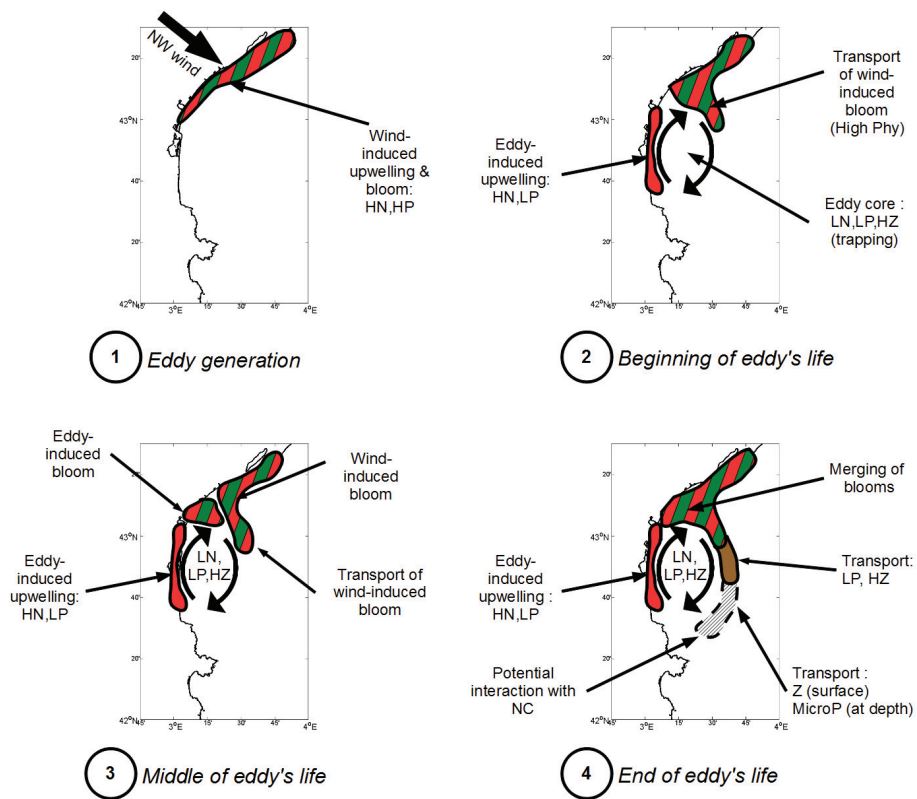


Figure 15: Temporal sequence of the schematic functioning of coastal eddies. H(L)N: high(low) nutrients concentrations, H(L)P: high(low) phytoplankton biomass, HZ: High zooplankton biomass, MicroP: microphytoplankton. Red areas are nutrient-enriched; green areas are phytoplankton-enriched; brown areas are zooplankton-enriched.

Appendix A. Model variables, equations, biogeochemical processes and parameters

Appendix A.1. List of state variables

Table A.1: List of state variables. X = C (carbon), N (nitrogen), P (phosphorus) or Si (silica)

Variables	Description	Unit
NO_3, NH_4, PO_4, SiO_4	Nitrate, Ammonium, Phosphate, Silicate	$mmol\ m^{-3}$
$XPhy_1, XPhy_2, XPhy_3$	Pico-, nano-, microphytoplankton in X	$mmol\ X\ m^{-3}$
$ChlPhy_1, ChlPhy_2, ChlPhy_3$	Pico-, nano-, micro- phytoplankton in chlorophyll	$mg\ Chl\ m^{-3}$
$XZoo_1, XZoo_2, CZoo_3$	Nano-, microzooplankton in X and meso-zooplankton in carbon	$mmol\ X\ m^{-3}$
$XBac$	Heterotrophic Bacteria in X	$mmol\ X\ m^{-3}$
DOX	Dissolved organic matter in X	$mmol\ X\ m^{-3}$
POX	Particulate organic matter in X	$mmol\ X\ m^{-3}$ or $mg\ Chl\ m^{-3}$

Appendix A.2. Biogeochemical fluxes and functions

Symbol	Definition	Units
$UptPhy_{i,Nut_j}$	Phytoplankton i uptake rate of nutrient Nut_j , $Nut_j = [NO_3, NH_4, PO_4, SiO_4]$	$mmol\ m^{-3}\ d^{-1}$
$ExuPhy_{i,DOX}$	Phytoplankton i exudation rate of dissolved organic matter DOX, $X = [C, N, P, SiO_4]$	$mmolX\ m^{-3}\ d^{-1}$
$MortPhy_{i,X}$	Phytoplankton i senescence rate in X, $X = [C, N, P, Si, Chl]$	$mmolX\ m^{-3}\ d^{-1}$
$Graz_{i,XPrey}$	Zooplankton i grazing rate on XPrey, $Prey = [Phy_i, Zoo_i, Bac]$, $X = [C, N, P, Chl, Si]$	$mmolX\ m^{-3}\ d^{-1}$
$MessyFeed_{3,X}$	Zooplankton 3 messy feeding rate in X, $X = [C, N, P]$	$mmolX\ m^{-3}\ d^{-1}$
$Eges_{3,X}$	Zooplankton 3 egestion rate in X, $X = [C, N, P, Si]$	$mmolX\ m^{-3}\ d^{-1}$
$ExuZoo_{i,DOX}$	Zooplankton i excretion rate of dissolved organic matter DOX, $X = [C, N, P]$	$mmolX\ m^{-3}\ d^{-1}$
gml_i	Growth multi-nutrient limitation function for zooplankton i	-
$(X/C)_{Zoo_i}$	Zooplankton i internal quota in X, $X = [N, P]$	$molX\ molC^{-1}$
f_{X,Zoo_i}^Q	Quota function for exudation and excretion of zooplankton i	-
$ExcZoo_{i,XNut}$	Zooplankton i excretion rate of dissolved inorganic matter XNut, $XNut = [NH_4, PO_4]$	$mmolN\ m^{-3}\ d^{-1}$ or $mmolP\ m^{-3}\ d^{-1}$
$MortZoo_{i,X}$	Zooplankton i mortality rate, $i = [1, 2]$	$mmolX\ m^{-3}\ d^{-1}$
$PredZoo_{3,X}$	Zooplankton 3 predation rate in X, $X = [C, N, P]$	$mmolX\ m^{-3}\ d^{-1}$
$UptBac_{DOX}$	Bacteria uptake rate of dissolved organic matter DOX, $X = [C, N, P]$	$mmolX\ m^{-3}\ d^{-1}$
gml	Growth multi-nutrient limitation function for bacteria	-
$UptBac_{XNut}$	Bacteria uptake rate of dissolved inorganic matter XNut, $XNut = [NH_4, PO_4]$	$mmolX\ m^{-3}\ d^{-1}$
$f_{X,Bac}^Q$	Quota function for uptake and release of nutrients and dissolved organic matter for bacteria	-
$(X/C)_{Bac}$	Bacteria internal quota in X, $X = [N, P]$	$molX\ molC^{-1}$
$RespBac$	Bacteria respiration rate	$mmolC\ m^{-3}\ d^{-1}$
$MortBac_X$	Bacteria mortality rate in X, $X = [C, N, P]$	$mmolX\ m^{-3}\ d^{-1}$
$Nitri_f$	Nitrification rate	$mmolN\ m^{-3}\ d^{-1}$
$f_{Phy_i}^T(T)$	Temperature function for phytoplankton processes	-
Rem_{POX}	Remineralisation of particulate organic matter POX, $X = [C, N, P]$	$mmolX\ m^{-3}\ d^{-1}$

Appendix A.3. Modified equations of the rates of change of the state variables

Zooplankton (Zoo_i $i = 1, 2$)

$$\xi_{CZoo_i} = \sum_{i=1}^2 Graz_{i,Cprey} - ExuZoo_{i,DOC} - MortZoo_{i,C} - \sum_{j>i} Graz_{j,CZoo_i}$$

$$\xi_{NZoo_i} = \sum_{i=1}^2 Graz_{i,Nprey} - ExuZoo_{i,DON} - ExuZoo_{i,NH_4} - MortZoo_{i,N} - \sum_{j>i} Graz_{j,NZoo_i}$$

$$\xi_{PZoo_i} = \sum_{i=1}^2 Graz_{i,Pprey} - ExuZoo_{i,DOP} - ExuZoo_{i,PO_4} - MortZoo_{i,P} - \sum_{j>i} Graz_{j,PZoo_i}$$

Picoheterotrophs (Bac)

$$\xi_{CBac_i} = \sum_{i=1}^2 Graz_{i,CBac} - uptBac_{i,DOC} - RespBac - MortBac_C$$

$$\xi_{NBac_i} = \sum_{i=1}^2 Graz_{i,NBac} - uptBac_{i,DON} - uptBac_{i,NH_4} - MortBac_N$$

$$\xi_{PBac_i} = \sum_{i=1}^2 Graz_{i,PBac} - uptBac_{i,DOP} - uptBac_{i,PO_4} - MortBac_P$$

Particulate organic matter (POM)

$X \in [C, N, P]$

$$\xi_{POX} = Eges_{3,X} + PredZoo_{3,X} + \sum_{i=1}^2 MortZoo_{i,X} + \sum_{i=1}^3 MortPhy_{i,X} - Rem_{POX}$$

$$\xi_{POSi} = Eges_{3,Si} + MortPhy_{3,Si} - Rem_{POSi}$$

$$\xi_{POchl} = \sum_{i=1}^3 Eges_{3,chl} + \sum_{i=1}^3 MortPhy_{i,chl} - Rem_{POchl}$$

Dissolved organic matter (DOM)

$$X \in [C, N, P]$$

$$\begin{aligned} \xi_{DOX} = & MessyFeed_{3,X} + \sum_{i=1}^3 ExuZoo_{i,DOX} + \sum_{i=1}^3 ExuPhy_{i,DOX} + MortBac_X + \\ & + Rem_{POX} - UptBac_{DOX} \end{aligned}$$

Dissolved inorganic matter (DIM)

$$\xi_{NH_4} = \sum_{i=1}^3 ExcZoo_{i,NH_4} - \sum_{i=1}^3 UptPhy_{i,NH_4} - UptBac_{NH_4} - Nitri_f$$

$$\xi_{PO_4} = \sum_{i=1}^3 ExcZoo_{i,PO_4} - \sum_{i=1}^3 UptPhy_{i,PO_4} - UptBac_{PO_4}$$

$$\xi_{SiO_4} = ExuPhy_{3,Si} + Rem_{POSi} - UptPhy_{3,Si}$$

Appendix A.4. Modified biogeochemical fluxes

Nano and micro-zooplankton

Exudation of DOC

$$ExuZoo_i,DOC = 1 - gml_i * Graz_i,CPrey$$

$$gml_i = \begin{cases} 0 & \text{if } (X_{lim}/C)_{Zoo_i} < (X_{lim}/C)_{Zoo_i}^{min} \\ 1 - \frac{(X_{lim}/C)_{Zoo_i}^{min}}{(X_{lim}/C)_{Zoo_1}} & \text{if } (X_{lim}/C)_{Zoo_i} \geq (X_{lim}/C)_{Zoo_i}^{min}. \end{cases}$$

Where X_{lim} is the limiting nutrient, $X \in [N, P]$, such that:

$$\frac{(X_{lim}/C)_{Zoo_i}}{(X_{lim}/C)_{Zoo_i}^{max}} = \min \left\{ \frac{(X_{lim}/C)_{Zoo_i}}{(X_{lim}/C)_{Zoo_i}^{max}} \right\}$$

Exudation of dissolved organic matter DOX $X \in [N, P]$

$$ExuZoo_i,DOX = fr_{DOX,Zoo_i}^{Exu} * (1 - fr_{X,Zoo_i}^Q) * Graz_i,XPrey$$

$$f_{X,Zoo_i}^Q = \begin{cases} \min \left\{ 1, \left(\frac{(X/C)_{Zoo_i}^{max} - (X/C)_{Zoo_i}}{(X/C)_{Zoo_i}^{max} - (X/C)_{Zoo_i}^{min}} \right)^{0.05} \right\} & \text{if } (X/C)_{Zoo_i} \leq (X/C)_{Zoo_i}^{max} \\ -\min \left\{ 1, \left(\frac{(X/C)_{Zoo_i}^{max} - (X/C)_{Zoo_i}}{(X/C)_{Zoo_i}^{max} - (X/C)_{Zoo_i}^{min}} \right)^{0.05} \right\} & \text{if } (X/C)_{Zoo_i} > (X/C)_{Zoo_i}^{max}. \end{cases}$$

Excretion of dissolved inorganic matter XNut $\in [NH_4, PO_4]$, $X \in [N, P]$

$$ExcZoo_i,XNut = (1 - fr_{DOX,Zoo_i}^{Exu}) * (1 - fr_{X,Zoo_i}^Q) * Graz_i,XPrey$$

Bacteria

Uptake of dissolved organic carbon

$$UptBac_{DOC} = \mu_{Bac} * \left(\frac{DOC}{DOC + k_{Bac,DOC}} \right) * CBac * gml * f_{Bac}^T(T)$$

$$gml = \begin{cases} 0 & \text{if } (X_{lim}/C)_{Bac} < (X_{lim}/C)_{Bac}^{min} \\ 1 - \frac{(X_{lim}/C)_{Bac}^{min}}{(X_{lim}/C)_{Bac}} & \text{if } (X_{lim}/C)_{Bac} \geq (X_{lim}/C)_{Bac}^{min}. \end{cases}$$

Where X_{lim} is the limiting nutrient, $X \in [N, P]$, such that:

$$\frac{(X_{lim}/C)_{Bac}}{(X_{lim}/C)_{Bac}^{max}} = \min \left\{ \frac{(X_{lim}/C)_{Bac}}{(X_{lim}/C)_{Bac}^{max}} \right\}$$

Uptake and release of dissolved organic matter $X \in [N, P]$

$$UptBac_{DOX} = \mu_{Bac} * \left(\frac{DOX}{DOX + k_{Bac,DOX}} \right) * (X/C)_{Bac}^{max} * CBac * f_{X,Bac}^Q * f_{Bac}^T(T)$$

$$f_{X,Bac}^Q = \begin{cases} \min \left\{ 1, \left(\frac{(X/C)_{Bac}^{max} - (X/C)_{Bac}}{(X/C)_{Bac}^{max} - (X/C)_{Bac}^{min}} \right)^{0.05} \right\} & \text{if } (X/C)_{Bac} \leq (X/C)_{Bac}^{max} \\ -\min \left\{ 1, \left(\frac{(X/C)_{Bac}^{max} - (X/C)_{Bac}}{(X/C)_{Bac}^{max} - (X/C)_{Bac}^{min}} \right)^{0.05} \right\} & \text{if } (X/C)_{Bac} > (X/C)_{Bac}^{max}. \end{cases}$$

Uptake and release of nutrients $XNut \in [NO_3, PO_4]$

$$UptBac_{XNut} = \mu_{Bac} * \left(\frac{XNut}{XNut + k_{Bac,XNut}} \right) * (X/C)_{Bac}^{max} * CBac * f_{X,Bac}^Q * f_{Bac}^T(T)$$

Respiration

$$Respbac = (1 - \omega_{bac}) * UptBac_{DOC}$$

Phytoplankton

Senescence $X \in [C, N, P, Chl, Si]$

$$Mort_{Phy_i, X} = \tau_{mort, Phy_i} * (1 - f_{Phy_i}^T(T)) * XPhy_i$$

$$f_{Phy_i}^T(T) = \max \left\{ 0, \frac{\left[2 * (1 - \beta_{Phy_i}) * \frac{T - T_{Phy_i}^{let}}{T_{Phy_i}^{opt} - T_{Phy_i}^{let}} \right]}{\left[\frac{T - T_{Phy_i}^{let}}{T_{Phy_i}^{opt} - T_{Phy_i}^{let}} \right]^2 + 2 * (\beta_{Phy_i}) * \left[\frac{T - T_{Phy_i}^{let}}{T_{Phy_i}^{opt} - T_{Phy_i}^{let}} \right] + 1} \right\}$$

Appendix A.5. Biogeochemical parameters

Symbol	Definition	Units	Values	References
Phytoplankton				
$\varphi_{max,Phyi}$	Maximum quantum yield	$mmolCJ^{-1}$	Phy1 2.88d ⁻⁵ Phy2 5.21d ⁻⁵ Phy3 2.03d ⁻⁴	1,2,c
$a_{chl,Phyi}$	Chl-specific absorption coeff.	m^2mgChl^{-1}	0.050	2
τ_{Phyi}	Renewal time of photosystems	s	2.0d ⁻³ 1.5d ⁻³ 1.0d ⁻³	3,c
σ_{Phyi}	Cross-section of photosystems	m^2J^{-1}	12.0	4,5,c
$k_d,Phyi$	Dimensionless PSII damage rate	-	2.6d ⁻⁸ 2.6d ⁻⁸ 2.6d ⁻⁸	6
$k_r,Phyi$	Rate of repair of damaged PSII	s^{-1}	2.0d ⁻⁴ 2.0d ⁻⁴ 2.0d ⁻⁴	6
$(N/C)_{Phyi}^{min}$	Minimal internal N:C quota	$molNmolC^{-1}$	0.138	7,8,9
$(N/C)_{Phyi}^{max}$	Maximal internal N:C quota	$molNmolC^{-1}$	0.194	7,8,9
$(P/C)_{Phyi}^{min}$	Minimal internal P:C quota	$molPmolC^{-1}$	0.0015	8,9,10,11
$(P/C)_{Phyi}^{max}$	Maximal internal P:C quota	$molPmolC^{-1}$	0.0068	8,9,10,11
$(Si/C)_{Phyi}^{min}$	Minimal internal Si:C quota	$molSimolC^{-1}$	-	9,11
$(Si/C)_{Phyi}^{max}$	Maximal internal Si:C quota	$molSimolC^{-1}$	-	9,11
$(Chl/N)_{Phyi}^{max}$	Maximal internal Chl:N quota	$mgChl molN^{-1}$	2.0	12,13,14
β_{Phyi}	Shape Coefficient for temperature curve	-	-0.50	15,c
T_{Phyi}^{let}	Lower lethal temperature	°C	11.0	15,c
T_{Phyi}^{opt}	Optimal temperature	°C	17.0	15,c
$k_{resp,Phyi}$	Respiration cost for growth	-	0.05	13,16,c
$k_{NO_3,Phyi}$	Half sat. constant for NO_3 uptake	$mmolNm^{-3}$	0.50	11,17,18,c
$k_{NH_4,Phyi}$	Half sat. constant for NH_4 uptake	$mmolNm^{-3}$	0.08	17,18,c
$k_{PO_4,Phyi}$	Half sat. constant for PO_4 uptake	$mmolPm^{-3}$	0.005	11,18,19,c
$k_{SiO_4,Phyi}$	Half sat. constant for Si uptake	$mmolSim^{-3}$	-	11,c
$k_{inhib,Phyi}$	Inhibition coefficient by NH_4	$mmolNm^{-3}$	0.005	17

Phytoplankton	Definition	Units	Values	References	
(cont.)					
$k_{q,Phy3}$	Constant in quota function for Si upt	$molNmolC^{-1}$	-	0.10	20
α_{Phy3}	Shape constant in quota function for Si upt	-	-	10.	20
$r_{NO_3,Phyi}$	Respiration cost for NO_3 uptake	$molCmolC^{-1}$	0.397	0.397	16
$r_{NH_4,Phyi}$	Respiration cost for NH_4 uptake	$molCmolC^{-1}$	0.198	0.198	16
$r_{PO_4,Phyi}$	Respiration cost for PO_4 uptake	$molCmolC^{-1}$	0.155	0.155	16
$r_{SiO_4,Phy3}$	Respiration cost for SiO_4 uptake	$molCmolC^{-1}$	-	0.140	16
$\tau_{mort,Phyi}$	Mortality rate	s^{-1}	-	$8.7d^{-7}$	21,c
$\omega_{s,Phyi}$	Sinking rate	ms^{-1}	-	$8.0d^{-6}$	15,c
Zooplankton	Definition	Units	Values	References	
g_{Zooi}	Maximum grazing rate	s^{-1}	$2.5d^{-5}$	$1.5d^{-5}$	22,23,c
ψ_{Zoo3}	Messy feeding constant	-	-	0.23	24
$k_{g,Zoo3}$	Half saturation constant	$mmolCm^{-3}$	5.0	20.0	25,c
β_{Zoo3}	Assimilation efficiency	-	-	0.70	24
$k_{resp,Zoo3}$	Respiration cost	-	-	0.20	24
$(N/C)_{Zoo3}$	Optimal internal N:C quota	$molNmolC^{-1}$	-	0.200	26,c
$(P/C)_{Zoo3}$	Optimal internal P:C quota	$molPmolC^{-1}$	-	0.013	26
$(N/C)_{Zoo_i^{min}}$	Minimal internal N:C quota	$molNmolC^{-1}$	0.122	0.066	27,28
$(N/C)_{Zoo_i^{max}}$	Maximal internal N:C quota	$molNmolC^{-1}$	0.158	0.214	27,28
$(P/C)_{Zoo_i^{min}}$	Minimal internal P:C quota	$molPmolC^{-1}$	0.0017	0.0370	c,28
$(P/C)_{Zoo_i^{max}}$	Maximal internal P:C quota	$molPmolC^{-1}$	0.0065	0.0119	c,28
$fr_{DOX,Zooi}^{Exu}$	exudation constant for DOM	-	0.53	0.53	29,c
$\tau_{mort,Zooi}$	Mortality rate	s^{-1}	$5.0d^{-7}$	$8.0d^{-7}$	c
$\tau_{mort,Zoo3}$	Predation rate	$m^3mmolC^{-1}s^{-1}$	-	$3.82d^{-7}$	21

Symbol	Definition	Units	Values	References
Bacteria				
μ_{Bac}	Maximum growth rate	s^{-1}	$9.69d^{-5}$	15,c
$k_{DOC,Bac}$	Half sat. constant for DOC uptake	$mmolCm^{-3}$	25	24
$k_{DON,Bac}$	Half sat. constant for DON uptake	$mmolNm^{-3}$	0.5	15
$k_{DOP,Bac}$	Half sat. constant for DOP uptake	$mmolPm^{-3}$	0.080	28
$k_{NH_4,Bac}$	Half sat. constant for NH4 uptake	$mmolNm^{-3}$	0.15	24,c
$k_{PO_4,Bac}$	Half sat. constant for PO4 uptake	$mmolPm^{-3}$	0.007	31,c
ω_{Bac}	Bacterial growth efficiency	-	0.20	24,c
$(N/C)_{Bac}^{min}$	Minimal internal N:C quota	$molNmolC^{-1}$	0.168	32
$(N/C)_{Bac}^{max}$	Maximal internal N:C quota	$molNmolC^{-1}$	0.264	32
$(P/C)_{Bac}^{min}$	Minimal internal P:C quota	$molPmolC^{-1}$	0.0083	32
$(P/C)_{Bac}^{max}$	Maximal internal P:C quota	$molPmolC^{-1}$	0.0278	32
$\tau_{mort,Bac}$	Mortality rate	s^{-1}	$5.0d^{-7}$	15
Q_{Bac}^{10}	Temperature Coefficient	-	2.95	26
T_{Bac}^{ref}	Reference Temperature	$^{\circ}C$	25	c
Non-living matter				
$\tau_{rem,POC}$	Remineralisation rate for POC	s^{-1}	$3.4d^{-7}$	24,c
$\tau_{rem,PON}$	Remineralisation rate for PON	s^{-1}	$0.58d^{-7}$	24,c
$\tau_{rem,POP}$	Remineralisation rate for POP	s^{-1}	$1.16d^{-7}$	31,c
$\tau_{rem,POSi}$	Remineralisation rate for POSi	s^{-1}	$3.86d^{-9}$	21

Non-living parameter (cont.)	Definition	Units	Values	References
$\tau_{rem,POchl}$	Remineralisation rate for Chlorophyll	s^{-1}	$1.16d^{-7}$	c
Q_{rem}^{10}	Temp. coefficient for remineralisation	-	2.95	26
T_{rem}^{ref}	Reference Temperature for remineralisation	$^{\circ}C$	25	c
$\tau_{rem,nitri}$	Temp. coefficient for nitrification	-	2.37	26
T_{nitri}^{ref}	Reference Temperature for nitrification	$^{\circ}C$	25	26
τ_{nitri}	Nitrification rate	s^{-1}	$5.91d^{-7}$	15,c
$W_{s,POM}$	Sinking rate of POM	ms^{-1}	$1.16d^{-5}$	15

Preferences	No Units				References
	Phy1	Phy2	Phy3	Zoo1	
Zoo1	0.20	0.30	-	-	Bac 22,c
Zoo2	0.07	0.20	0.09	0.44	- 30,c
Zoo3	-	0.10	0.40	0.15	- 23,c

References: (c) calibration; (1) Babin et al. (1996); (2) Claustre et al. (2005); (3) Laney et al. (2005); (4) Moore et al. (2003); (5) Gorbunov et al. (1999); (6) Oliver et al. (2003); (7) Heldal et al. (2003); (8) Riegman et al. (2000); (9) Geider et al. (1998); (10) Bertilsson et al. (2003); (11) Sarthou et al. (2005); (12) Geider et al. (1997); (13) Nielsen (1997); (14) Moore et al. (2004); (15) Lacroix and Grégoire (2002); (16) Thornley and Cannell (2000); (17) Harrison et al. (1996); (18) Tyrrell and Taylor (1996); (19) Timmermans et al. (2005); (20) Davidson and Gurney (1999); (21) Fasham et al. (2006); (22) Christaki et al. (2002); (23) Nejtgaard et al. (1997); (24) Anderson and Pondaven (2003); (25) Hansen et al. (1997); (26) Vichi et al. (2007); (27) Putt and Stoecker (1989); (28) Eccleston-Parry and Leadbeater (1995); (29) Vincent et al. (2007); (30) Liu and Dagg (2003); (31) Thingstad et al. (1993); (32) Vrede et al. (2002).